Computational Mechanics 34 (2004) 510–531 © Springer-Verlag 2004
DOI 10.1007/s00466-004-0598-5

Three dimensional Voronoi cell finite element model for microstructures with ellipsoidal heterogeneties

S. Ghosh S. Moorthy

Abstract In this paper a three-dimensional Voronoi cell finite element model is developed for analyzing heterogeneous materials containing a dispersion of ellipsoidal inclusions or voids in the matrix. The paper starts with a description of 3D tessellation of a domain with ellipsoidal heterogeneities, to yield a 3D mesh of Voronoi cells containing the heterogeneities. A surface based tessellation algorithm is developed to account for the shape and size of the ellipsoids in point based tessellation methods. The 3D Voronoi cell finite element model, using the assumed stress hybrid formulation, is developed for determining stresses and displacements in a linear elastic material domain. Special stress functions that introduce classical Lamé functions in ellipsoidal coordinates are implemented to enhance solution convergence. Numerical methods for implementation of algorithms and yielding stable solutions are discussed. Numerical examples are conducted with inclusions and voids to demonstrate the effectiveness of the model.

Keywords Voronoi cell Finite Element Model, Tessellation, Hybrid stress formulation, Ellipsoids

1 Introduction

Advanced heterogeneous materials are increasingly finding more use in various engineering applications. The materials may be metals or alloys with microscopic precipitates and pores or composites containing a dispersion of fibers, whiskers or particulates. The heterogeneities in the matrix play an important role on the overall structural behavior. Robust analytical and numerical models are necessary for predicting effective properties and stresses and strains in the microstructure for these materials. A number of micromechanical studies have been reported in the literature on heterogeneous materials containing inclusions and voids. Analytical methods for determining stress fields around a spherical cavity in an infinite domain have been developed in Timoshenko and Goodier [1]. Sadowsky and Sternberg have analyzed stress concentration around an ellipsoidal cavity using ellipsoidal coordinates in [2, 3], and around two spherical cavities using bispherical coordinates in [3]. Chen and Acrivos [5] have utilized the Boussinesq-Papkovich stress functions for stress analysis of an infinite domain with two spherical cavities and rigid inclusions. Chen and Young [6] have proposed approximations using integral equations for voids or inclusions of arbitrary shapes in an elastic medium. While these analytical micro-mechanical models are powerful, their effectiveness is generally limited to simple geometries and low volume fractions.

Various numerical micromechanical approaches have been developed for a more versatile evaluation of microstructural stresses and strains and overall behavior. Numerical unit cell models using the finite element method or boundary element methods, have been proposed e.g. in [7,8]. Rodin and Hwang have numerically studied a finite number of spherical inhomogeneities in an infinite region [9]. Recently three dimensional multi-particle models have been developed by Gusev [10] for elastic particle reinforced composites using tetrahedral finite elements, and by Michel, Moulinec and Suquet [12] using Fast Fourier Transform methods. Böhm et al. [13, 14], Segurado and Llorca [15] and Zohdi [11] have developed 3D elastic-plastic models for dispersion of multiple particles in metal matrix composites with ductile matrix. Moes et. al. [16] have developed an elegant *XFEM* model for 3D elastic composite microstructures. A software package Palmyra [17] has been developed to design composite materials and to calculate physical properties of heterogeneous materials.

The 2-D Voronoi cell finite element model (VCFEM) has been developed for elastic and elastic-plastic micromechanical problems in composite and porous materials in [18, 19, 20], and for damage initiation in reinforced composites by particle cracking in [21, 20]. The model evolves by Voronoi tessellation of the microstructure to generate a morphology based network of multi-sided Voronoi cells, each cell containing a heterogeneity. Each cell is treated as a FEM element and requires no additional discretization. VCFEM incorporates assumptions from micromechanics theories, as well as adaptive enhancements. This model has been shown to require significantly reduced degrees of freedom compared to displacement based FEM models and are hence computationally efficient.

The extension of VCFEM to 3D is a nontrivial enterprise due to different characteristic micromechanical solutions and differences in geometric considerations. In this paper,

Received: 20 Feburary 2004 / Accepted: 17 May 2004
Published online: 20 July 2004

S. Ghosh (✉)
Department of Mechanical Engineering
The Ohio State University Columbus,
OH USA e-mail: ghosh.5@osu.edu

S. Moorthy
Department of Civil Engineering
Louisiana State University, LA USA

a 3D VCFEM model is developed for elastic materials with ellipsoidal inclusions or voids. The paper starts with discussion of the Voronoi tessellation algorithm for mesh generation, accounting for shapes, sizes and locations of heterogeneities. The VCFEM formulation is then developed introducing special stress functions in ellipsoidal coordinates to explicitly account for shape. Various aspects of numerical implementation of the model are subsequently discussed with attention on stability and accuracy of the solutions. Finally a number of numerical examples are solved for model validation and for modeling multi-inclusion microstructures.

2
Three dimensional mesh generation by tessellation into Voronoi cells

Discretization of 3D heterogeneous domains, containing particles or voids, into a mesh of polyhedra is the first step in the development of the 3D Voronoi cell finite element model. Each of the Voronoi cells in this construct contains a single heterogeneity at most. This section describes a 3D tessellation algorithm from the general definition of Voronoi diagrams. The corresponding 2D algorithms have been described in [22]. Following the mathematical description given in [23], the Voronoi diagram is used to geometrically subdivide a region, based on a set of seed points. Let $P = \{p_1, ..p_i..., p_n; 2 \leq n < \infty\}$ represent a set of n independent points dispersed in the 3D space with coordinates $x_i \neq x_j \in \Re^3$, $\forall i \neq j; i, j \in I_n$. The region

$$V(p_i) = \{x : \| x - x_i \| \leq \| x - x_j \| \ \forall j \neq i, j \in I_n\} \qquad (1)$$

represents a Voronoi polyhedron associated with the point $p_i \subset \Re^3$. Thus a Voronoi polyhedron associated with generator p_i encompasses all points whose distances to p_i are less than their distances to any other point p_j. Each polyhedron is the intersection of open half spaces bounded by perpendicular bisectors of lines joining a generator p_i with each of its neighbors p_j, a property that renders the polytopes convex. The boundary segment $\mathbf{B_{ij}}$, common to polyhedra for seed points p_i and p_j, are nearer to them than to any other labeled point in the domain. This is denoted as

$$\mathbf{B_{ij}} = \{x : \| x - x_i \| = \| x - x_j \| \leq \| x - x_k \| \quad \forall\ k \neq i, j\} \qquad (2)$$

Also the vertex $\mathbf{V_{ijk}}$ of the polyhedron is equidistant from three or more generating points p_i, p_j and p_k

$$\mathbf{V_{ijk}} = \{\mathbf{x} : \| \mathbf{x} - \mathbf{x_i} \| = \| \mathbf{x} - \mathbf{x_j} \| = \| \mathbf{x} - \mathbf{x_k} \| \leq \| \mathbf{x} - \mathbf{x_l} \| \quad \forall \mathbf{l} \neq \mathbf{i}, \mathbf{j}, \mathbf{k}\} \qquad (3)$$

The aggregate of all polyhedra, represented by the set $\mathcal{V} = \{V(p_1), \ldots, V(p_n)\}$ represents a Voronoi diagram or mesh generated for the point set P in 3-dimensional space. If the distribution of the point set is uniform in space, the Voronoi cells reduce to uniform rectangular hexahedrons.

2.1
Algorithm for point based tessellation

Kumar [24] has given a comprehensive account of several algorithms to delineate 3D Voronoi tessellations based on point generators. Kiang [25], Andrade [26] have generated a finite number of grid points in the 3D spatial domain and have considered grid points nearest to a generating point (or seed) P to be a part of the Voronoi cell generated by the point P. Mahin et al. [27] have used a recursive algorithm, in which the information on minimum and maximum times to reach and leave a cubic volume for each generator, is used to assign volume to a generator or to divide further into sub-volumes. Another algorithm, developed by Mackay [28], Finney [29], Tanaka [30] and others is based on finding all centers of spheres passing through any four generators by solving a system of 4 quadratic equations. The centers of these spheres are possible sites of the Voronoi cell vertices in the mesh. Hinde and Miles [31], Pathak [32] and Winterfeld [33] have proposed algorithms in which the nearest neighbors are found such that the in-center of a sphere passing through neighboring generators falls on the perpendicular bisector of the plane joining the generators.

The tessellation algorithm developed in this paper is based on Winterfeld's algorithm [33]. The perpendicular bisector plane $B_{ij}(\hat{r}_{ij})$ between point $p_i(\hat{r}_i)$ and $p_j(\hat{r}_j)$, depicted in the figure 1a, is described as

$$(\hat{r}_i - \hat{r}_j) \cdot \left(\hat{r}_{ij} - \frac{\hat{r}_i + \hat{r}_j}{2}\right) = 0 \ , \qquad (4)$$

where $\hat{r}_{ij}$ is the position vector of any point $\hat{p}_{ij}(x, y, z)$ in the plane B_{ij}. Equation (4) may be rewritten in terms of the Cartesian coordinates as

$$a_{ij}x + b_{ij}y + c_{ij}z = d_{ij} \ , \qquad (5)$$

where $a_{ij} = x_i - x_j$, $b_{ij} = y_i - y_j$, $c_{ij} = z_i - z_j$, $d_{ij} = \frac{1}{2}((x_i - x_j)(x_i + x_j) + (y_i - y_j)(y_i + y_j) + (z_i - z_j)(z_i + z_j))$. Analysis domains of many heterogeneous materials are prismatic in shape, often with 6 bounding planes. The domain boundaries in these cases are described by bisector planes that are constructed by assigning a set of virtual neighboring generators mirrored about the boundary planes. Basic steps in constructing the mesh of Voronoi polyhedra from a set of generating points in 3D space are described below.

1. Identify the neighboring points for a given generator p_i. The space surrounding the point p_i is divided into eight octants and the N points closest to p_i in each octant are selected. The number N is generally selected as 10 for accuracy and efficiency [33]. Following this, the bisector planes between a generator p_i and each of the $8N$ neighbors ($p_j; j = 1 \cdots 8N$) are constructed using Eq. (5). These $8N$ bisector planes, together with the 6 bounding planes of the prism are considered as candidates for faces of the Voronoi polyhedron associated with a generator p_i.
2. Construct the edges of the polyhedra in a sequential manner, starting with p_j the nearest neighbor to p_i. The

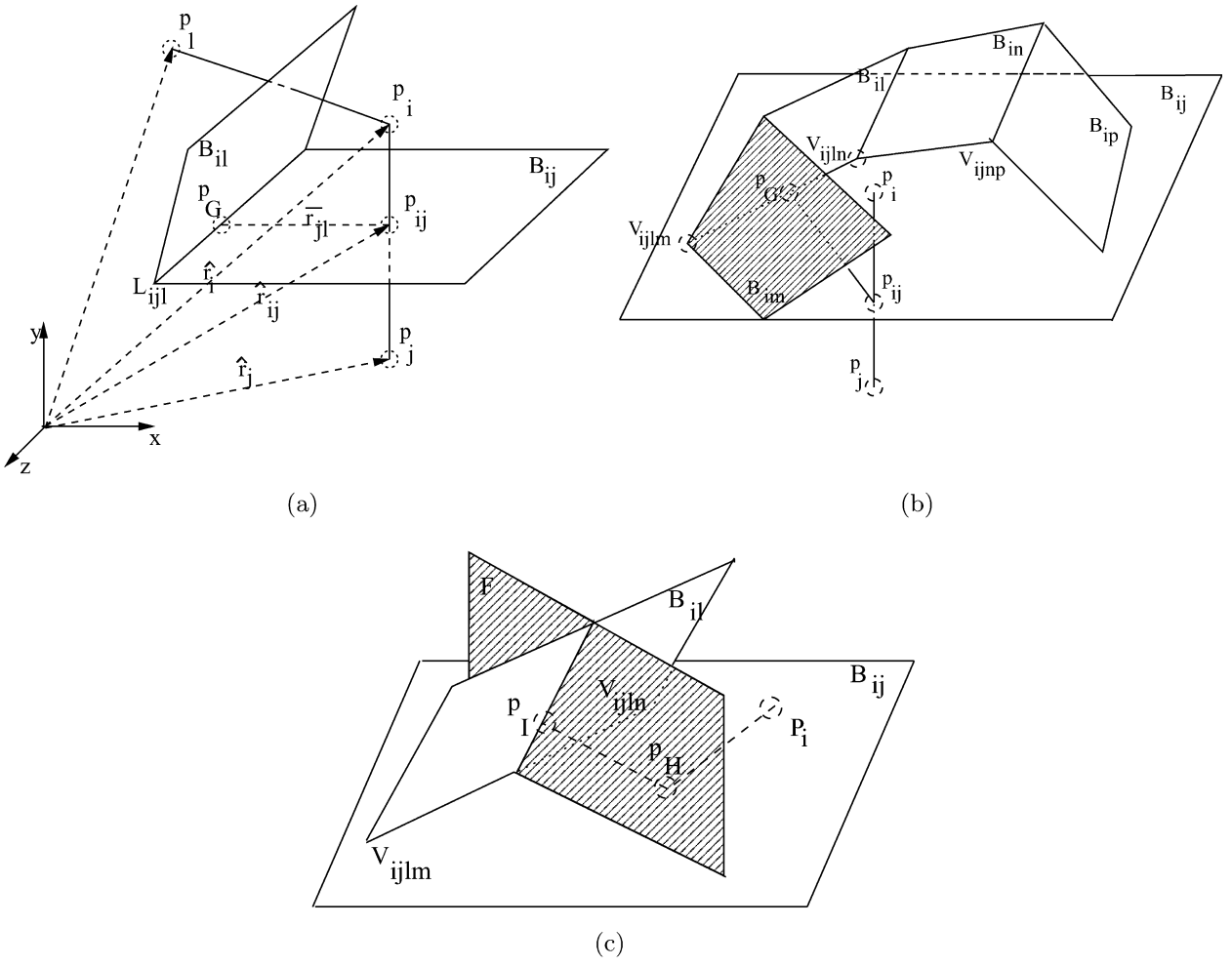

Fig. 1. (a) Bisector and first plane and line of polyhedron i (b) Construction of the first edge (c) Location of the pivoting point. p_I

first polyhedron face is a sub-domain of the bisector plane B_{ij}. Point p_{ij} in the bisector plane B_{ij}, defined by the position vector $\hat{r}_i + \hat{r}_j/2$, is utilized in realizing the boundary of the face. The edge L_{ijl} of the face B_{ij}, shown in figure 1, corresponds to a boundary of the Voronoi cell associated with the generator p_i and is constructed from the $8N - 1 + 6$ possible neighbors. Here 6 corresponds to the number of bounding planes. For each neighbor $p_l (l \neq j)$ and the 6 bounding planes, the edge line $L_{ijl}(\hat{r}_{ijl})$ is formed as the intersection of the bisector or boundary planes B_{ij} and B_{il} i.e., $L_{ijl} : B_{ij} \cap B_{il} \forall j \neq l$. The plane B_{il} that is chosen as the first face of the Voronoi polyhedron, is the one for which the perpendicular distance $\bar{r}_{jl} = (\hat{r}_{ij} - \hat{r}_{jl})$ from the point p_{ij} to the edge L_{ijl} is a minimum as shown in Fig. 1a. The intersecting line L_{ijl} is obtained by solving the simultaneous algebraic equations for the bisector planes:

$$a_{ij}x_G + b_{ij}y_G + c_{ij}z_G = d_{ij}, a_{il}x_G + b_{il}y_G + c_{il}z_G = d_{il} \tag{6}$$

The point p_{ijl}, which is the shortest distance on L_{ijl} from p_{ij}, is obtained by solving an additional constraint equation:

$$(\hat{n}_{ij} \times \hat{n}_{il}) \cdot (\hat{r}_{ij} - \hat{r}_G) = 0 \tag{7}$$

Here $\hat{n}_{ij}$ and $\hat{n}_{il}$ are normals to bisector planes B_{ij} and B_{il} respectively and $\hat{n}_{ij} \times \hat{n}_{il}$ is the direction of the line L_{ijl}. This yields the relation

$$(b_{ij}c_{il} - c_{ij}b_{il})(x_G - x_F) + (c_{ij}a_{il} - a_{ij}c_{il})$$
$$(y_G - y_F) + (a_{ij}b_{il} - b_{ij}a_{il})(z_G - z_F) = 0 \tag{8}$$

The coordinates of the point $P_G(x_G, y_G, z_G)$ are obtained by solving equations (6) and (8).

3. Delineate the limits of the first edge L_{ijl}, corresponding to the vertices of the Voronoi cell for the generator p_i. These are the intersection of the line L_{ijl} with neighboring bisector planes, generated from neighbors p_m and p_n. As illustrated in Fig. 1b, the vertices V_{ijln} and V_{ijlm}, are obtained as the intersection of the line L_{ijl} with the bisector planes B_{im} and B_{in} for $m, n \neq i, j, l$. For any point $p_k (k \neq i, j, l)$ the vertex V_{ijkl} is generated as the intersection of bisector planes B_{ik}, B_{il} and B_{ij} by solving the corresponding equations

$$a_{ik}x + b_{ik}y + c_{ik}z = d_{ik}, a_{il}x + b_{il}y + c_{il}z = d_{il} \ ,$$
$$a_{ij}x + b_{ij}y + c_{ij}z = d_{ij} \tag{9}$$

These are constructed using the points p_i, p_k, p_l and p_j. Points p_m and p_n are chosen from $(8N - 2 + 6)$ points

so that $|\hat{r}_{ijlm} - \hat{r}_G|$ and $|\hat{r}_{ijln} - \hat{r}_G|$ are the minimum distances from P_G to all vertices in both directions. The positive and negative directions along the line L_{ijl}, from P_G to the vertices are chosen from the conditions

$$(\hat{r}_F - \hat{r}_i) \cdot \left[(\hat{r}_{ijlm} - \hat{r}_{ij}) \times (\hat{r}_G - \hat{r}_{ij})\right] < 0$$
$$(\hat{r}_F - \hat{r}_i) \cdot \left[(\hat{r}_{ijln} - \hat{r}_{ij}) \times (\hat{r}_G - \hat{r}_{ij})\right] > 0 \qquad (10)$$

respectively. Each line L_{ijl}, terminating with the vertices V_{ijlm} and V_{ijln} constitutes an edge of a polygon designated as E_{ijlmn}. Of the subscripts, i corresponds to the generating point, j and l correspond to the neighboring points contributing to the edge L_{ijl}, and m and n correspond to the generators of the limit plane.

4. Subsequently, construct the other edges in a sequential manner. Faces are constructed to close the polyhedron using the property, that two faces share every edge in each closed polyhedron.
5. The bisector point p_{ij} is considered as a central point in the construction of all edges, e.g. E_{ijlmn}, in the plane B_{ij}. After constructing the first edge E_{ijlmn}, subsequent edges E_{ijlmp} are constructed in the direction of right-hand rule with the thumb pointing from p_j to p_i. The next vertex V_{ijnp} for the generator p_p is chosen such that the vector $(\hat{r}_{ij} - \hat{r}_i) \cdot (\hat{r}_{ijnp} - \hat{r}_{ij}) \times (\hat{r}_{ijnp} - \hat{r}_{ij})$ has the same sign as $(\hat{r}_{ij} - \hat{r}_i) \cdot \left[(\hat{r}_{ijlm} - \hat{r}_{ij}) \times (\hat{r}_{ijlm} - \hat{r}_{ij})\right]$. Furthermore, the vertex V_{ijnp} is selected from all $8N - 4 + 6$ possible candidate bisector planes such that the distance $\left|\hat{r}_{ijln} - \hat{r}_{ijnp}\right|$ is a minimum. The process of generating adjacent vertices and edges is continued until the last vertex coincides with the starting vertex V_{ijlm}.
6. Upon construction of the polygonal face $F_{ij} \subset B_{ij}$ for the point p_i, other faces of the Voronoi polyhedron, e.g. $F_{il} \subset B_{il}$, are generated by using the same algorithm. Note that the two vertices V_{ijlm} and V_{ijln} and edge E_{ijlmn} have already been determined. The other vertices are then determined as the intersection of the plane B_{il} with another candidate bisector plane following the steps enumerated next and depicted in figure 1c.

   (a) Generate a plane F that is perpendicular to the plane B_{il} ($F \perp B_{il}$) and a bisector of the edge E_{ijlmn} ($F \perp E_{ijlmn}$), satisfying the condition $(\hat{r}_m - \frac{\hat{r}_{ijlm} + \hat{r}_{ijln}}{2}) \cdot (\hat{r}_{ijln} - \hat{r}_{ijln}) = 0$ resulting in

   $$a_m x + b_m y + c_m z = d_m \qquad (11)$$

   where

   $$a_m = x_{ijlm} - x_{ijln}, b_m = y_{ijlm} - y_{ijln}, c_m = z_{ijlm} - z_{ijln},$$
   $$d_m = \frac{1}{2}\left[(x^2_{ijlm} - x^2_{ijln}) + (y^2_{ijlm} - y^2_{ijln}) + (z^2_{ijlm} - z^2_{ijln})\right] \qquad (12)$$

   (b) From p_i, drop a perpendicular on the plane F, intersecting the latter at point p_H. The point p_H may be obtained from a directional line Eq. [34], by solving the equations

   $$\frac{x_H - x_i}{a_m} = \frac{y_H - y_i}{b_m} = \frac{z_H - z_i}{c_m},$$
   $$a_m x_H + b_m y_H + c_m z_H = d_m \qquad (13)$$

   where a_m, b_m, c_m, d_m are determined in Eq. (11) and (12).

   (c) From p_H, drop a perpendicular on plane B_{il} to intersect at the point p_I.

   (d) The location of p_I with respect to the edge E_{ijlmn} is important in determining the directional sequence of vertices of the face F_{il}. A reference point p_I' on the line containing point p_I and the middle point of edge E_{ijlmn} is constructed very close to the edge E_{ijlmn} and on the same side as the point p_I. The sign of the vector operation

   $$(\hat{r}_{I'} - \hat{r}_i) \cdot \left[(\hat{r}_{ijlm} - \hat{r}_{I'}) \times (\hat{r}_{ijln} - \hat{r}_{I'})\right]$$

   is used to determine the directional sequence. The rest of the construction follows steps $1 - 5$.
7. After the first face of polyhedron is constructed about generator p_i, the other faces are constructed from edges of the first face till the entire polyhedron is closed.

2.2 Surface based Voronoi tessellation for ellipsoidal heterogeneities

The VCFEM mesh is based on Voronoi tessellation of the microstructure consisting of finite sized heterogeneities. If the heterogeneities are equi-sized non-intersecting spheres, the resulting Voronoi polyhedra are the same as those generated by the point generation methods with their centroids as generators. However, most physical domains contain nonuniform heterogeneities of different sizes and shapes. Intersection of the bisector planes with heterogeneities may be a common occurrence with the centroid-based tessellation algorithms for these cases. Consequently, a surface-based algorithm is developed based on bisector planes between closest points on the surface of two neighboring ellipsoids. In this algorithm, closest points $p_i'(x_i', y_i', z_i')$ and $p_j'(x_j', y_j', z_j')$ between two neighboring ellipsoids are first obtained by solving a constrained minimization problem:

$$\text{Minimize} : f(x_i', y_i', z_i', x_j', y_j', z_j') = (x_j' - x_i')^2 + (y_j' - y_i')^2 + (z_j' - z_i')^2$$
$$wrt\ x_i', y_i', z_i', x_j', y_j', z_j'$$

such that the points belong to the ellipsoidal surfaces:

$$\frac{\hat{x}_i^2}{a_i^2} + \frac{\hat{y}_i^2}{b_i^2} + \frac{\hat{z}_i^2}{c_i^2} = 1, \quad \frac{\hat{x}_j^2}{a_j^2} + \frac{\hat{y}_j^2}{b_j^2} + \frac{\hat{z}_j^2}{c_j^2} = 1 \qquad (14)$$

where

$$\begin{Bmatrix} \hat{x}_i \\ \hat{y}_i \\ \hat{z}_i \end{Bmatrix} = [R_i] \begin{Bmatrix} x_i' - x_i \\ y_i' - y_i \\ z_i' - z_i \end{Bmatrix}$$

Here (x_i, y_i, z_i) and (x_j, y_j, z_j) are ellipsoidal centroidal coordinates, a_i, b_i, c_i and a_j, b_j, c_j are the semi-axes and $[R_i]$ and $[R_j]$ are the coordinate transformation matrices from global coordinate system to local coordinate systems, of the two ellipsoids. The local coordinate system has its origin at the centroid of the ellipsoid with the three axis

aligned with the three principal axes. The corresponding unconstrained minimization problem is constructed by using Lagrange multipliers as,

$$F(x_i', y_i', z_i', x_j', y_j', z_j', \lambda_1, \lambda_2) = (x_j' - x_i')^2 + (y_j' - y_i')^2 + (z_j' - z_i')^2 + \lambda_1\left(\frac{\hat{x}_i^2}{a_i^2} + \frac{\hat{y}_i^2}{b_i^2} + \frac{\hat{z}_i^2}{c_i^2} - 1\right) + \lambda_2\left(\frac{\hat{x}_j^2}{a_j^2} + \frac{\hat{y}_j^2}{b_j^2} + \frac{\hat{z}_j^2}{c_j^2} - 1\right)$$

The minimum distance is obtained by the solving the minimization Equation [35,36] as

$$\nabla F_k = 0 \Rightarrow \frac{\partial \bar{F} b}{\partial s_k} = 0 \ (k = 1 \ldots 8) \tag{15}$$

where s_k is the set of 6 coordinates for the two closest points and the 2 Lagrange multipliers.

A serious problem that may arise with surface based algorithms is the non-concurrence of three candidate intersecting edges, i.e. they do not meet at a point. This is illustrated in Fig. 2a. The non-concurrent edges form a small triangular region *ABC* in Fig. 2b, which would reduce to a point in the point-based tessellation algorithm. Consequently, the triangular domain is shrunk to a point with coordinates determined by averaging those of the vertices of the triangle. The method rotates the corresponding edges slightly. The vertex merging process is done sequentially. Intersection of edges with heterogeneities is subsequently checked and local perturbations are made to avoid these intersections. An alternative to this is to allow non-planar edges, which was avoided in this paper.

Heterogeneous domains with various spherical and ellipsoidal inclusions are tessellated into 3D Voronoi cell meshes using the code developed. The resulting meshes are tested for edge intersection with heterogeneities as well as for internal voids or overlaps. For the latter check, the sum of the individual volumes of all Voronoi cells is compared with the volume of the heterogeneous domain in consideration. Selected tessellated domains, shown in Fig. 3, include: (a) 100 randomly distributed spheres of the same size with volume fraction 15% and (b) 100 randomly distributed ellipsoids of different sizes with 1 cluster with volume fraction 15%, all in a $10 \times 10 \times 4$ box. The results of the tessellation are found to be satisfactory for all these cases.

3 The 3D Voronoi cell FEM (VCFEM) formulation

Each Voronoi cell with the included heterogeneity constitutes an element in the 3D Voronoi cell finite element model. In each Voronoi element, the matrix and heterogeneity phases are denoted as Ω_e^M and Ω_e^I respectively. The element boundary $\partial\Omega_e^E$ is comprised of three mutually disjoint parts, namely the prescribed traction boundary Γ_{te}, the prescribed displacement boundary Γ_{ue}, and the inter-element boundary Γ_{me}. Thus $\partial\Omega_e^E = \Gamma_{te} \bigcup \Gamma_{ue} \bigcup \Gamma_{me}$. The interface $\partial\Omega_e^I$ between the matrix and heterogeneity has an outward normal $\mathbf{n}^I$, and $\mathbf{n}^E$ is the outward normal to $\partial\Omega_e^E$. For the VCFEM element formulation for heterogeneous materials, the micromechanics boundary value problem is described as:

$$\begin{aligned}
&\text{Find}(\boldsymbol{\sigma}^M, \boldsymbol{\sigma}^I, \mathbf{u}^E, \mathbf{u}^I) \in \mathcal{T}^M \times \mathcal{T}^I \times \mathcal{V}^E \times \mathcal{V}^I \text{ satisfying} \\
&\nabla \cdot \boldsymbol{\sigma}^M + \bar{\mathbf{f}}^M = \mathbf{0} \in \Omega^M \text{ and } \nabla \cdot \boldsymbol{\sigma}^I + \mathbf{f}^I = \mathbf{0} \in \Omega^I \quad \text{(a)} \\
&\frac{\partial B^M}{\partial \boldsymbol{\sigma}^M} = \boldsymbol{\epsilon}^M \in \Omega^M \text{ and } \frac{\partial B^I}{\partial \boldsymbol{\sigma}^I} = \boldsymbol{\epsilon}^I \in \Omega^I \quad \text{(b)} \\
&\mathbf{u}^E = \bar{\mathbf{u}} \text{ on } \Gamma_{ue} \text{ and } \boldsymbol{\sigma}_e^M \cdot \mathbf{n}^E = \bar{\mathbf{t}} \text{ on } \Gamma_{te} \quad \text{(c)}
\end{aligned} \tag{16}$$

The variables $\boldsymbol{\sigma}$, $\boldsymbol{\epsilon}$, B and $\mathbf{f}$ are the equilibriated stress fields, the corresponding strain fields, the complimentary energy and body forces per unit volume respectively in the element interior. $\mathbf{u}^E$ and $\mathbf{u}^I$ are the compatible displacement fields on the boundary $\partial\Omega_e^E$ and the matrix-heterogeneity interface $\partial\Omega_e^I$. Variables with superscripts M and I correspond to the interior of the matrix and inclusion phases respectively, while superscript E refers to variables on the element boundary. The superscript I is also used to denote quantities on the matrix-inclusion interface. $\mathcal{T}^M, \mathcal{T}^I, \mathcal{V}^E, \mathcal{V}^I$ correspond to Hilbert spaces

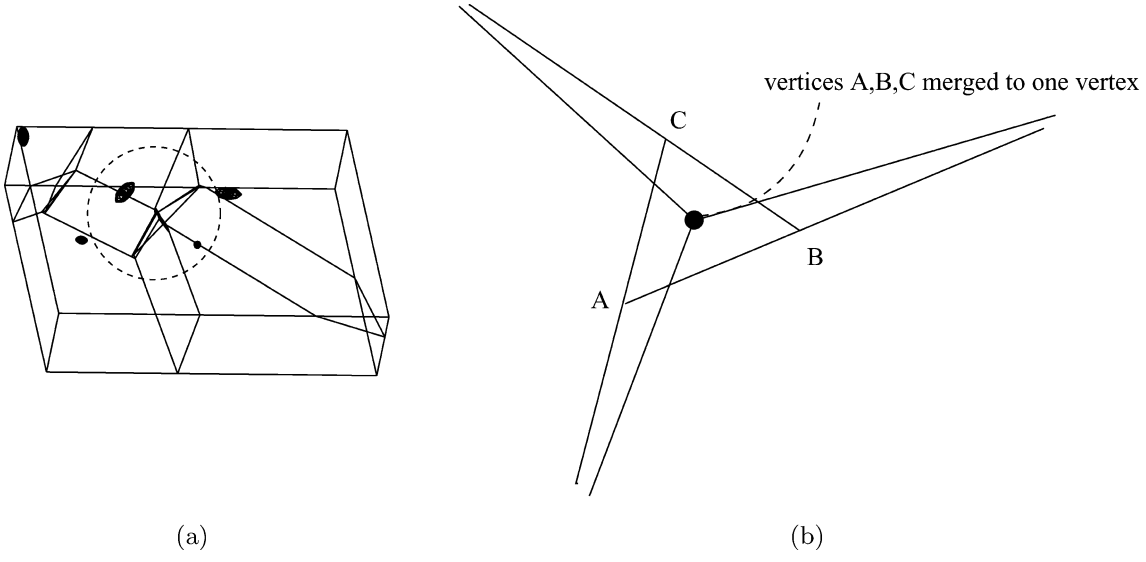

Fig. 2. (a) Problems caused by using surface based bisectors (b) Solution obtained by merging of vertices

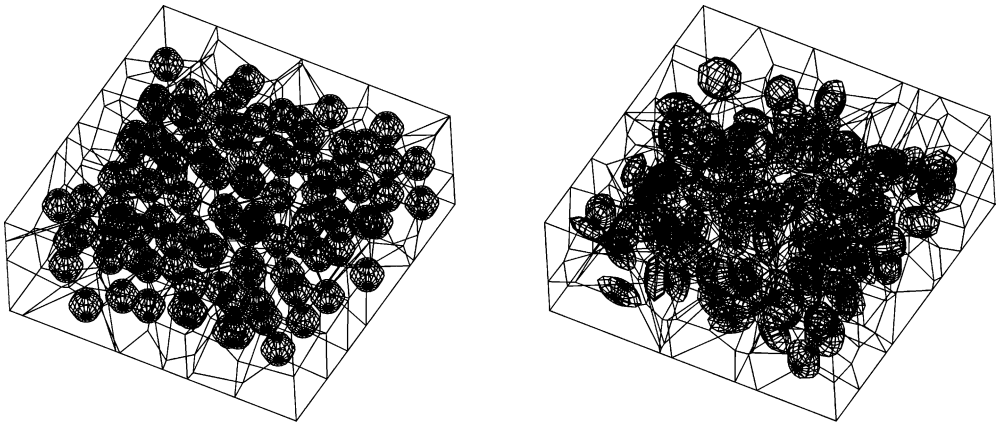

(a) (b)

Fig. 3. Tessellated domains yielding Voronoi cell meshes for (a) 100 randomly distributed spheres of the same size with volume fraction 15% and (b) 100 randomly distributed ellipsoids of different sizes with 1 cluster with volume fraction 15%

containing the stress and displacement solutions respectively. The VCFEM formulation is based on the assumed stress hybrid finite element method, in which stationarity conditions of the element energy functional $\sum_{e=1}^{N} \Pi_e(\boldsymbol{\sigma}^M, \boldsymbol{\sigma}^I, \mathbf{u}^E, \mathbf{u}^I)$ in the variational principle yields the weak forms of the kinematic equation and traction reciprocity conditions, as Euler equations. In the small deformation elasticity finite element formulation, the element energy functional Π_e is defined in terms of stresses and boundary and interface displacement fields as:

$$\begin{aligned}\Pi_e(\boldsymbol{\sigma}_e^M, \boldsymbol{\sigma}_e^I, \mathbf{u}_e^E, \mathbf{u}_e^I) = &- \int_{\Omega_e^M} B^M(\boldsymbol{\sigma}_e^M) d\Omega \\ &- \int_{\Omega_e^I} B^I(\boldsymbol{\sigma}_e^I) d\Omega \\ &+ \int_{\partial\Omega_e^E} \boldsymbol{\sigma}_e^M \cdot \mathbf{n}^E \cdot \mathbf{u}_e^E d\partial\Omega \\ &- \int_{\Gamma_{tE}} \bar{\mathbf{t}} \cdot \mathbf{u}_e^E d\Gamma \\ &- \int_{\partial\Omega_e^I} (\boldsymbol{\sigma}_e^M - \boldsymbol{\sigma}_e^I) \cdot \mathbf{n}^I \cdot \mathbf{u}_e^I d\partial\Omega \quad (17)\end{aligned}$$

The element complimentary energy density B is expressed in terms of the equilibriated stresses as $B = \frac{1}{2}\boldsymbol{\sigma} : \mathbf{S} : \boldsymbol{\sigma}$, with $\mathbf{S}$ as the compliance matrix. The element energy functional consists of bilinear forms ${}_e a^{M/I}$, ${}_e b_{E/I}^{M/I}$ and the linear functionals ${}_e f^E$ and ${}_e g^{M/I}$ defined as

$$\begin{aligned}&{}_e a^{M/I}(\boldsymbol{\sigma}_e^{M/I}, \tau_e^{M/I}) = \int_{\Omega_e^{M/I}} \frac{\partial B_e^{M/I}}{\partial \boldsymbol{\sigma}_e{}^{M/I}} : \tau_e^{M/I} d\Omega \\ &\times_e a^{M/I} : \mathcal{T}_e^{M/I} \times \mathcal{T}_e^{M/I} \to \mathcal{R} \\ &\times_e b_{E/I}^{M/I}(\boldsymbol{\sigma}_e^{M/I}, \mathbf{u}_e^{E/I}) = \int_{\partial\Omega_e^{E/I}} \boldsymbol{\sigma}_e^{M/I} \cdot \mathbf{n}_e^{E/I} \cdot \mathbf{u}_e^{E/I} d\Omega \\ &\times_e b_{E/I}^{M/I} : \mathcal{T}_e^{M/I} \times \mathcal{V}_e^{E/I} \to \mathcal{R} \\ &\times_e f^E(\mathbf{u}_e^E) = \int_{\Gamma_{te}} \bar{\mathbf{t}}.\mathbf{u}_e^E d\Gamma \qquad {}_e f^E : \mathcal{V}_e^E \to \mathcal{R} \\ &\times_e g^{M/I}(\boldsymbol{\sigma}_e^{M/I}) = \int_{\Omega_e^{M/I}} \frac{\partial B_e^{M/I}}{\partial \boldsymbol{\sigma}_e{}^{M/I}} : \boldsymbol{\sigma}_e^{M/I} d\Gamma \\ &\times_e g^{M/I} : \mathcal{T}_e^{M/I} \to \mathcal{R} \qquad (18)\end{aligned}$$

The (/) symbol is used to denote alternative domains, e.g. M/I corresponds to the interior of the matrix or inclusion. In VCFE formulation, the equilibrium conditions and constitutive relations in both the matrix and inclusion phases, and the compatibility conditions on the element boundary and matrix-inclusion interface are satisfied a-priori in a strong sense. The element kinematic equations in the matrix and inclusion phases, i.e.

$$\nabla \mathbf{u}_e^M = \boldsymbol{\epsilon}_e^M \text{ in } \Omega_e^M \text{ and } \nabla \mathbf{u}_e^I = \boldsymbol{\epsilon}_e^I \text{ in } \Omega_e^I \qquad (19)$$

are however satisfied in a weak sense from the stationary conditions of the element energy functional in equation(17). The weak forms are obtained by setting the first variation of Π_e with respect to stresses in individual phases to zero as

$$\begin{aligned}&-_e a^M(\boldsymbol{\sigma}_e^M, \delta\boldsymbol{\sigma}_e^M) +_e b_E^M(\delta\boldsymbol{\sigma}_e^M, \mathbf{u}_\mathbf{e}^\mathbf{E}) -_\mathbf{e} \mathbf{b}_\mathbf{I}^\mathbf{M}(\delta\boldsymbol{\sigma}_\mathbf{e}^\mathbf{M}, \mathbf{u}_\mathbf{e}^\mathbf{I}) \\ &\quad = 0 \quad \forall \delta\boldsymbol{\sigma}_e^M \in \mathcal{T}_e^M, \forall e \\ &-_e a^I(\boldsymbol{\sigma}_e^I, \delta\boldsymbol{\sigma}_e^I) +_e b_I^I(\delta\boldsymbol{\sigma}_e^I, \mathbf{u}_\mathbf{e}^\mathbf{I}) \\ &\quad = 0 \quad \forall \delta\boldsymbol{\sigma}_e^I \in \mathcal{T}_e^I, \forall e \qquad (20)\end{aligned}$$

Solution of Eq. (20) yields stresses in the constituent phases. Furthermore, the VCFE formulation assumes weak satisfaction of the traction reciprocity conditions on the (i) the matrix-inclusion interface $\partial\Omega_e^I$, (ii) the inter-element boundary Γ_{me}, and (iii) the domain traction boundary Γ_{te}, expressed as:

$$\begin{aligned}&\boldsymbol{\sigma}_e^I \cdot \mathbf{n}^I = \boldsymbol{\sigma}_e^M \cdot \mathbf{n}^I \text{ on } \partial\Omega_e^I(\text{interface}) \\ &\boldsymbol{\sigma}_e^M \cdot \mathbf{n}^{E+} = -\boldsymbol{\sigma}_e^M \cdot \mathbf{n}^{E-} \text{ on } \partial\Omega_e^E(\text{inter-element boundary}) \\ &\boldsymbol{\sigma}_e^M \cdot \mathbf{n}^E = \bar{\mathbf{t}} \text{ on } \Gamma_{te}(\text{traction boundary}) \qquad (21)\end{aligned}$$

In the variational principle, the weak form is obtained by setting the first variation of the total energy functional $\Pi = \sum_{e=1}^{N} \Pi_e$ with respect to the displacements on the element boundaries and interfaces to zero as:

$$\begin{aligned}&\sum_{e=1}^{N} {}_e b_E^M(\boldsymbol{\sigma}_e^M, \delta\mathbf{u}_e^E) = \sum_{e=1}^{N} {}_e f^E(\delta\mathbf{u}_e^E) \quad \forall \delta\mathbf{u}_e^E \in \bar{\mathcal{V}}_e^E \\ &\quad = \{\mathbf{v}_e^E \in \mathcal{H}^o(\partial\Omega_e^E) : \mathbf{v}^E = \mathbf{0} \text{ on } \Gamma_{ue}\} \forall e \\ &\qquad \times_e b_I^I(\boldsymbol{\sigma}_e^I, \delta\mathbf{u}_e^I) -_e b_I^M(\boldsymbol{\sigma}_e^M, \delta\mathbf{u}_e^I) = 0 \quad \forall \delta\mathbf{u}_e^I \in \mathcal{V}_e^I, \forall e \\ &\qquad (22)\end{aligned}$$

3.1
Equilibriated stress fields in VCFEM

In the absence of body forces, three dimensional stress fields satisfying equilibrium relations can be generated in terms of components of an appropriately chosen symmetric tensor stress function $\Phi_{ij}(x_1, x_2, x_3)(= \Phi_{ji}(x_1, x_2, x_3)$ (see [37, 38]). The resulting stresses are

$$\begin{aligned}
\sigma_{11} &= \frac{\partial^2\Phi_{22}}{\partial x_3^2} + \frac{\partial^2\Phi_{33}}{\partial x_2^2} - 2\frac{\partial^2\Phi_{23}}{\partial x_2\partial x_3} \\
\sigma_{22} &= \frac{\partial^2\Phi_{33}}{\partial x_1^2} + \frac{\partial^2\Phi_{11}}{\partial x_3^2} - 2\frac{\partial^2\Phi_{31}}{\partial x_1\partial x_3} \\
\sigma_{33} &= \frac{\partial^2\Phi_{11}}{\partial x_2^2} + \frac{\partial^2\Phi_{22}}{\partial x_1^2} - 2\frac{\partial^2\Phi_{12}}{\partial x_1\partial x_2} \\
\sigma_{12} &= \frac{\partial^2\Phi_{23}}{\partial x_1\partial x_3} + \frac{\partial^2\Phi_{13}}{\partial x_2\partial x_3} - \frac{\partial^2\Phi_{12}}{\partial x_3^2} - \frac{\partial^2\Phi_{33}}{\partial x_1\partial x_2} \\
\sigma_{13} &= \frac{\partial^2\Phi_{12}}{\partial x_2\partial x_3} + \frac{\partial^2\Phi_{23}}{\partial x_1\partial x_2} - \frac{\partial^2\Phi_{13}}{\partial x_2^2} - \frac{\partial^2\Phi_{22}}{\partial x_1\partial x_3} \\
\sigma_{23} &= \frac{\partial^2\Phi_{13}}{\partial x_1\partial x_2} + \frac{\partial^2\Phi_{12}}{\partial x_1\partial x_3} - \frac{\partial^2\Phi_{23}}{\partial x_1^2} - \frac{\partial^2\Phi_{11}}{\partial x_2\partial x_3}
\end{aligned} \tag{23}$$

The six scalar stress functions Φ_{ij} are not independent. Two reductions of the full matrix representation of Φ_{ij} are commonly known as the Maxwell and Morera's stress functions [37,38] and are expressed as

$$\textbf{Maxwell} : \Phi_{ij} = 0 \ \ \forall \ \ i \neq j \text{ and } \textbf{Morera} : \Phi_{ij} = 0 \ \ \forall \ \ i = j$$

It is possible to construct a set of Maxwell or Morera functions for every stress distribution that satisfies the equilibrium Eqs.[37]. Different functional forms of the stress functions are chosen for the matrix and inclusion phases in VCFEM implementation. Independent choices of $\Phi_{ij}^M(x_1, x_2, x_3)$ and $\Phi_{ij}^I(x_1, x_2, x_3)$ allow for stress discontinuities across the matrix-inclusion interface. It is important to note that the stresses can vary significantly inside of each element, depending on the choice of stress functions. Substitution of these functions in Eq.(23) yields stresses in terms of well defined functions of the position [**P**] and unknown stress coefficients $\boldsymbol{\beta}$ as:

$$\begin{aligned}
\{\boldsymbol{\sigma}_e^M\} &= [\mathbf{P}^M(x_1, x_2, x_3)]\{\boldsymbol{\beta}_e^M\}, \\
\{\boldsymbol{\sigma}_e^I\} &= [\mathbf{P}^I(x_1, x_2, x_3)]\{\boldsymbol{\beta}_e^I\}
\end{aligned} \tag{24}$$

Convergence properties and efficiency of VCFEM are significantly affected by the choice of Φ_{ij}. These functions should adequately account for the shape, size and location of the heterogeneity in the element. Interface effects should be strong in its vicinity, but should decay with increasing distance from it. Polynomial functions alone do not contribute adequately to this requirement and hence suffers from poor convergence [18]. Consequently, stress functions in VCFEM are constructed from two sets of expansion functions that have complementary effects on the solution convergence.

3.1.1
Pure polynomial forms of stress functions:
The components of the stress functions Φ_{ij}^M and Φ_{ij}^I are constructed using pure polynomial expressions in terms of the location (x_1, x_2, x_3), as.:

$$\begin{aligned}
(\Phi_{poly}^M)_{ij} &= \sum_{p,q,r} (\beta^M)_{pqr}^{ij} x_1^p x_2^q x_3^r \text{ and} \\
(\Phi_{poly}^I)_{ij} &= \sum_{p,q,r} (\beta^I)_{pqr}^{ij} x_1^p x_2^q x_3^r
\end{aligned} \tag{25}$$

As discussed in [39], invariance of stresses with respect to coordinate transformations can be ensured by a complete polynomial representation of Φ_{ij}. Stability of the algorithm requires linear independence of the columns of basis functions $[\mathbf{P}^M(x_1, x_2, x_3)]$ and $[\mathbf{P}^I(x_1, x_2, x_3)]$. A special procedure is implemented for constructing the three dependent components in either the Maxwell or the Morera stress functions that would satisfy linear independence of $[\mathbf{P}(x_1, x_2, x_3)]$.

1. Stresses $\boldsymbol{\sigma}_e^{M/I}$ are constructed from only the first component $\Phi_{11}(x_1, x_2, x_3)$, using Eq. (23) and (25).
2. The next set of stresses are constructed using $\Phi_{22}(x_1, x_2, x_3)$ in Eq. (23).
3. The two sets of stresses from steps 1 and 2 are compared to seek out terms with identical exponents in the terms containing $x_1^i x_2^j$ and x_3^k. The corresponding coefficients, e.g. $(\beta^{M/I})_{ijk}^{22}$ in Φ_{22} are set to zero.
4. This procedure is repeated with all the other components of Φ_{ij} in sequence.

3.1.2
Reciprocal stress functions based on interface geometry:
It has been demonstrated with 2D VCFEM in [18] that very high order terms are required with pure polynomials to account for the effects of the matrix-inclusion or void interface, leading to poor convergence. To avert this, reciprocal augmentation functions have been developed in [18,19] following the analytical solutions of Muskhelishvili [40]. In 3D, a novel method of developing reciprocal stress functions is developed to improve convergence. The method follows displacement solutions in an isotropic elastic domain with an ellipsoidal cavity developed by Sadowsky and Sternberg [2, 3]. The 3D general solutions to Navier's equation for elastic media, as proposed by Boussinesq, is obtained by superposition of four harmonic solutions [1]

$$\begin{aligned}
2G[u_1, u_2, u_3]^{X_1} &= x_1\left[\frac{\partial X_1}{\partial x_1}, \frac{\partial X_1}{\partial x_2}, \frac{\partial X_1}{\partial x_3}\right] \\
&\quad - [(3-4\nu)X_1, 0, 0] && \text{(a)} \\
2G[u_1, u_2, u_3]^{X_2} &= x_2\left[\frac{\partial X_2}{\partial x_1}, \frac{\partial X_2}{\partial x_2}, \frac{\partial X_2}{\partial x_3}\right] \\
&\quad - [0, (3-4\nu)X_2, 0] && \text{(b)} \\
2G[u_1, u_2, u_3]^{X_3} &= x_3\left[\frac{\partial X_3}{\partial x_1}, \frac{\partial X_3}{\partial x_2}, \frac{\partial X_3}{\partial x_3}\right] \\
&\quad - [0, 0, (3-4\nu)X_3] && \text{(c)} \\
2G[u_1, u_2, u_3]^{F} &= \left[\frac{\partial F}{\partial x_1}, \frac{\partial F}{\partial x_2}, \frac{\partial F}{\partial x_3}\right] && \text{(d)}
\end{aligned} \tag{26}$$

where G is the shear modulus, and $X_i (i = 1, 2, 3)$ and F are harmonic functions, satisfying the Laplace equations.

Stress fields are generated by superposing stress solutions (26) using the generalized Hooke's law. The stress solutions for each of the displacements are

$$\begin{Bmatrix}\sigma_{11}\\ \sigma_{22}\\ \sigma_{33}\\ \sigma_{12}\\ \sigma_{31}\\ \sigma_{23}\end{Bmatrix}^{X_1} = \begin{Bmatrix} -2(1-v)\frac{\partial X_1}{\partial x_1} + x_1\frac{\partial^2 X_1}{\partial x_1^2} \\ -2v\frac{\partial X_1}{\partial x_1} + x_1\frac{\partial^2 X_1}{\partial x_2^2} \\ -2v\frac{\partial X_1}{\partial x_1} + x_1\frac{\partial^2 X_1}{\partial x_3^2} \\ -(1-2v)\frac{\partial X_1}{\partial x_2} + x_1\frac{\partial^2 X_1}{\partial x_1\partial x_2} \\ -(1-2v)\frac{\partial X_1}{\partial x_3} + x_1\frac{\partial^2 X_1}{\partial x_1\partial x_3} \\ x_1\frac{\partial^2 X_1}{\partial x_3\partial x_2} \end{Bmatrix} \text{from equation (26a)} \tag{27}$$

$$\begin{Bmatrix}\sigma_{11}\\ \sigma_{22}\\ \sigma_{33}\\ \sigma_{12}\\ \sigma_{31}\\ \sigma_{23}\end{Bmatrix}^{X_2} = \begin{Bmatrix} -2v\frac{\partial X_2}{\partial x_2} + x_2\frac{\partial^2 X_2}{\partial x_1^2} \\ -2v\frac{\partial X_2}{\partial x_2} + x_2\frac{\partial^2 X_2}{\partial x_2^2} \\ -2v\frac{\partial X_2}{\partial x_2} + x_2\frac{\partial^2 X_2}{\partial x_3^2} \\ -(1-2v)\frac{\partial X_2}{\partial x_1} + x_2\frac{\partial^2 X_2}{\partial x_1\partial x_2} \\ x_2\frac{\partial^2 X_2}{\partial x_1\partial x_3} \\ -(1-2v)\frac{\partial X_2}{\partial x_3} + x_2\frac{\partial^2 X_2}{\partial x_2\partial x_3} \end{Bmatrix} \text{from equation (26b)} \tag{28}$$

$$\begin{Bmatrix}\sigma_{11}\\ \sigma_{22}\\ \sigma_{33}\\ \sigma_{12}\\ \sigma_{31}\\ \sigma_{23}\end{Bmatrix}^{X_3} = \begin{Bmatrix} -2v\frac{\partial X_3}{\partial x_3} + x_3\frac{\partial^2 X_3}{\partial x_1^2} \\ -2v\frac{\partial X_3}{\partial x_3} + x_3\frac{\partial^2 X_3}{\partial x_2^2} \\ -2(1-v)\frac{\partial X_3}{\partial x_1} + x_3\frac{\partial^2 X_3}{\partial x_3^2} \\ x_3\frac{\partial^2 X_3}{\partial x_1\partial x_2} \\ -(1-2v)\frac{\partial X_3}{\partial x_1} + x_3\frac{\partial^2 X_3}{\partial x_1\partial x_3} \\ -(1-2v)\frac{\partial X_3}{\partial x_2} + x_3\frac{\partial^2 X_3}{\partial x_2\partial x_3} \end{Bmatrix} \text{from equation (26c)} \tag{29}$$

$$\begin{Bmatrix}\sigma_{11}\\ \sigma_{22}\\ \sigma_{33}\\ \sigma_{12}\\ \sigma_{31}\\ \sigma_{23}\end{Bmatrix}^{F} = \begin{Bmatrix} \frac{\partial^2 F}{\partial x_1^2} \\ \frac{\partial^2 F}{\partial x_2^2} \\ \frac{\partial^2 F}{\partial x_3^2} \\ \frac{\partial^2 F}{\partial x_1\partial x_2} \\ \frac{\partial^2 F}{\partial x_1\partial x_3} \\ \frac{\partial^2 F}{\partial x_2\partial x_3} \end{Bmatrix} \text{from equation (26d)} \tag{30}$$

Each of the above stress fields satisfies equilibrium equations. Consequently, stress functions $\Phi_{ij}(i=j=1,2,3)$, for representing equilibriated stress fields in Eq. (23), can be derived from these stress fields. For example, stresses from Maxwell stress functions corresponding to the displacement solutions X_1, can be written as

$$\sigma_{11}^{X_1} = \frac{\partial^2\Phi_{22}^{X_1}}{\partial x_3^2} + \frac{\partial^2\Phi_{33}^{X_1}}{\partial x_2^2},\ \sigma_{22}^{X_1} = \frac{\partial^2\Phi_{33}^{X_1}}{\partial x_1^2} + \frac{\partial^2\Phi_{11}^{X_1}}{\partial x_3^2},$$

$$\sigma_{33}^{X_1} = \frac{\partial^2\Phi_{11}^{X_1}}{\partial x_2^2} + \frac{\partial^2\Phi_{22}^{X_1}}{\partial x_1^2}$$

$$\sigma_{12}^{X_1} = -\frac{\partial^2\Phi_{33}^{X_1}}{\partial x_1\partial x_2},\ \sigma_{13}^{X_1} = -\frac{\partial^2\Phi_{22}^{X_1}}{\partial x_1\partial x_3},$$

$$\sigma_{23}^{X_1} = -\frac{\partial^2\Phi_{11}^{X_1}}{\partial x_2\partial x_3} \tag{31}$$

The functional forms of stress function components are assumed as follows

$$\Phi_{11}^{X_1} = -x_1X_1,\ \Phi_{22}^{X_1} = \Phi_{33}^{X_1} = -x_1X_1 + 2(1-v)\int X_1dx_1 \tag{32}$$

the corresponding stresses can be derived from Eqs. (31), (32) and (26) as

$$\sigma_{11}^{X_1} = -x_1\left(\frac{\partial^2 X_1}{\partial x_2^2} + \frac{\partial^2 X_1}{\partial x_3^2}\right) + 2(1-v) \times \int\left(\frac{\partial^2 X_1}{\partial x_2^2} + \frac{\partial^2 X_1}{\partial x_3^2}\right)dx_1 = x_1\frac{\partial^2 X_1}{\partial x_1^2} - 2(1-v)\frac{\partial X_1}{\partial x_1}$$

$$\sigma_{22}^{X_1} = -x_1\frac{\partial^2 X_1}{\partial x_3^2} - 2\frac{\partial X_1}{\partial x_1} - x_1\frac{\partial^2 X_1}{\partial x_1^2} + 2(1-v)\frac{\partial X_1}{\partial x_1} = -x_1\left(\frac{\partial^2 X_1}{\partial x_3^2} + \frac{\partial^2 X_1}{\partial x_1^2}\right) - 2v\frac{\partial X_1}{\partial x_1} = x_1\frac{\partial^2 X_1}{\partial x_2^2} - 2v\frac{\partial X_1}{\partial x_1}$$

$$\sigma_{33}^{X_1} = x_1\frac{\partial^2 X_1}{\partial x_3^2} - 2v\frac{\partial X_1}{\partial x_1}$$

$$\sigma_{12}^{X_1} = -\frac{\partial}{\partial x_2}\left[-X_1 - x_1\frac{\partial X_1}{\partial x_1} + 2(1-v)X_1\right] = -\left[(1-2v)\frac{\partial X_1}{\partial x_2} - x_1\frac{\partial^2 X_1}{\partial x_1\partial x_2}\right]$$

$$\sigma_{13}^{X_1} = \left[(1-2v)\frac{\partial X_1}{\partial x_2} - x_1\frac{\partial^2 X_1}{\partial x_1\partial x_2}\right]$$

$$\sigma_{23}^{X_1} = x_1\frac{\partial^2 X_1}{\partial x_2\partial x_3} \tag{33}$$

These are exactly the same as stress expressions in Eqs. (27). Stress functions from the other functions in the set (27, 28, 29, 30), are constructed as

$$\Phi_{11}^{X_2} = \Phi_{33}^{X_2} = -x_2X_2 + 2(1-\nu)\int X_2 dx_2,\ \Phi_{22}^{X_2} = -x_2X_2$$

$$\Phi_{11}^{X_3} = \Phi_{22}^{X_3} = -x_3X_3 + 2(1-\nu)\int X_3 dx_3,\ \Phi_{33}^{X_3} = -x_3X_3$$

$$\Phi_{11}^{F} = \Phi_{22}^{F} = \Phi_{33}^{F} = -F \tag{34}$$

These stress functions should satisfy necessary displacement constraints at the interface, as well as facilitate stress concentration. To accomplish this, a set of harmonic displacement potential functions X_1, X_2, X_3 and F that vanish at infinity is chosen. These functions are periodic and are symmetric with respect to the principal ellipsoidal coordinates α_1, α_2 and α_3. In [3], displacement potentials X_1, X_2, X_3 and F have been expressed as Lame functions of the first and second kind to satisfy these conditions. These functions are expressed in terms of ellipsoidal coordinates $(\alpha_1, \alpha_2, \alpha_3)$ as

$$X_1 = mS_1s_2s_3, X_2 = -\frac{m}{k'}C_1c_2c_3,$$

$$X_3 = -\frac{im}{k^2k'}D_1d_2d_3, \tag{35}$$

where (s_j, c_j, d_j) and (S_j, C_j, D_j), $(j = 1, 2, 3)$ are elliptical functions of the first and second kind respectively (see Hobson [41]), m is a constant that depends on the dimensions of the ellipsoid and $i = \sqrt{-1}$. Let $(\hat{x}_1, \hat{x}_2, \hat{x}_3)$ correspond to an orthogonal coordinate system centered at the centroid and along the principal directions of the ellipsoid. The ellipsoidal coordinates $\alpha_j(\hat{x}_1, \hat{x}_2, \hat{x}_3), j = 1, 2, 3$ may be derived to satisfy the characteristic equations

$$\frac{\hat{x}_1^2}{\alpha_1^2} + \frac{\hat{x}_2^2}{\alpha_1^2 - h^2} + \frac{\hat{x}_3^2}{\alpha_1^2 - k^2} = 1 \,\forall\, k^2 \le \alpha_1^2 \le \infty \tag{a}$$

$$\frac{\hat{x}_1^2}{\alpha_2^2} + \frac{\hat{x}_2^2}{\alpha_2^2 - h^2} - \frac{\hat{x}_3^2}{k^2 - \alpha_2^2} = 1 \,\forall\, h^2 \le \alpha_2^2 \le k^2 \tag{b}$$

$$\frac{\hat{x}_1^2}{\alpha_3^2} - \frac{\hat{x}_2^2}{h^2 - \alpha_3^2} - \frac{\hat{x}_3^2}{k^2 - \alpha_3^2} = 1 \,\forall\, 0 \le \alpha_3^2 \le h^2 \tag{c}$$

(36)

For $\alpha_1 = constant$, Eq. (36a) reduces to that of an ellipsoid. If $\alpha_2 = constant$ in Eq. (36b), it yields the equation of a hyperboloid of 1 sheet, and if $\alpha_3 = constant$ in Eq. (36c), it yields the equation of a hyperboloid of 2 sheets. The Eqs. in (36) can be solved to obtain a set of possible Cartesian coordinates $(\hat{x}_1, \hat{x}_2, \hat{x}_3)$ in terms of the ellipsoidal coordinates $(\alpha_1, \alpha_2, \alpha_3)$ as

$$\hat{x}_1 = \frac{\alpha_1\alpha_2\alpha_3}{hk},\ \hat{x}_2 = \frac{\sqrt{(\alpha_1^2 - h^2)}\sqrt{(\alpha_2^2 - h^2)}\sqrt{(h^2 - \alpha_3^2)}}{h\sqrt{(k^2 - h^2)}},$$

$$\hat{x}_3 = \frac{\sqrt{(\alpha_1^2 - k^2)}\sqrt{(k^2 - \alpha_2^2)}\sqrt{(k^2 - \alpha_3^2)}}{k\sqrt{(k^2 - h^2)}} \tag{37}$$

Lame functions used in [3] can be expressed in terms of the ellipsoidal coordinates (see [41]) as

$$s_1 = \alpha_1/h,\ s_2 = \alpha_2/h,\ s_3 = \alpha_3/h \tag{a}$$

$$c_1 = \sqrt{\alpha_1^2 - h^2},\ c_2 = \sqrt{\alpha_2^2 - h^2},\ c_3 = \sqrt{h^2 - \alpha_3^2} \tag{b}$$

$$d_1 = \sqrt{\alpha_1^2 - k^2}, d_2 = \sqrt{k^2 - \alpha_2^2},\ d_3 = \sqrt{k^2 - \alpha_3^2} \tag{c}$$

$$S_1 = 3\alpha_1\int_{\alpha_1}^{\infty}\frac{d\alpha_1}{\alpha_1^2\sqrt{(\alpha_1^2 - h^2)}\sqrt{(\alpha_1^2 - k^2)}} \tag{d}$$

$$C_1 = 3\sqrt{\alpha_1^2 - h^2}\int_{\alpha_1}^{\infty}\frac{d\alpha_1}{(\alpha_1^2 - h^2)^{\frac{3}{2}}\sqrt{(\alpha_1^2 - k^2)}} \tag{e}$$

$$D_1 = 3\sqrt{\alpha_1^2 - k^2}\int_{\alpha_1}^{\infty}\frac{d\alpha_1}{(\alpha_1^2 - k^2)^{\frac{3}{2}}\sqrt{(\alpha_1^2 - h^2)}} \tag{f}$$

(38)

The above functions may be expressed in terms of the standard elliptic integrals of the first kind (ε^I) and the second kind (ε^{II}), that are defined as,

$$\varepsilon^I(t, K) = \int_0^t \frac{dz}{\sqrt{1 - K^2z^2}\sqrt{1 - z^2}} \text{ and}$$

$$\varepsilon^{II}(t, K) = \int_0^t \frac{\sqrt{1 - z^2}dz}{\sqrt{1 - K^2z^2}} \tag{39}$$

Consequently, functions in Eq. (38) can be expressed in terms of elliptic integrals in Eq. (39) (see [42,43]) as:

$$S_1 = 3s_1\left((\varepsilon^I\left(\frac{k}{\alpha_1}, \frac{h}{k}\right) - \varepsilon^{II}\left(\frac{k}{\alpha_1}, \frac{h}{k}\right)\right)h^2$$

$$= s_1\left(A_1^1 * \varepsilon^I\left(\frac{k}{\alpha_1}, \frac{h}{k}\right) + A_2^1 * \varepsilon^{II}\left(\frac{k}{\alpha_1}, \frac{h}{k}\right) + A_3^1\right)$$

$$C_1 = 3s_2\left(-\left(1 - \frac{h^2}{k^2}\right)\varepsilon^{II}\left(\frac{k}{\alpha_1}, \frac{h}{k}\right) + \varepsilon^I\left(\frac{k}{\alpha_1}, \frac{h}{k}\right)\right.$$

$$\left. - \frac{h^2}{k\sqrt{\alpha_1^2 - h^2}}\sqrt{1 - \left(\frac{k}{\alpha_1}\right)^2}\right)\frac{hk}{\sqrt{k^2 - h^2}}$$

$$= c_1\left(A_1^2 * \varepsilon^I\left(\frac{k}{\alpha_1}, \frac{h}{k}\right) + A_2^2 * \varepsilon^{II}\left(\frac{k}{\alpha_1}, \frac{h}{k}\right) + A_3^2\right)$$

$$D_1 = 3s_3\left(\frac{k}{\sqrt{\alpha_1^2 - k^2}}\sqrt{1 - \frac{h^{2^2}}{\alpha_1}} - \varepsilon^I\left(\frac{k}{\alpha_1}, \frac{h}{k}\right)\right)\frac{h^2}{\sqrt{k^2 - h^2}}$$

$$= d_1\left(A_1^3 * \varepsilon^I\left(\frac{k}{\alpha_1}, \frac{h}{k}\right) + A_2^3 * \varepsilon^{II}\left(\frac{k}{\alpha_1}, \frac{h}{k}\right) + A_3^3\right)$$

(40)

The detailed expressions for A_i^j are given in the appendix. The superscript j in A_i^j corresponds to the respective Lame functions $s_1(j = 1)$, $c_1(j = 2)$ and $d_1(j = 3)$. The displacement potentials are then obtained by substituting Eqs. (40) and (37) in Eq. (35), i.e.

$$X_1 = \hat{x}_1\left(A_1^1 * \varepsilon^I\left(\frac{k}{\alpha_1}, \frac{h}{k}\right) + A_2^1 * \varepsilon^{II}\left(\frac{k}{\alpha_1}, \frac{h}{k}\right) + A_3^1\right)$$

$$X_2 = \hat{x}_2\left(A_1^2 * \varepsilon^I\left(\frac{k}{\alpha_1}, \frac{h}{k}\right) + A_2^2 * \varepsilon^{II}\left(\frac{k}{\alpha_1}, \frac{h}{k}\right) + A_3^2\right)$$

$$X_3 = \hat{x}_3\left(A_1^3 * \varepsilon^I\left(\frac{k}{\alpha_1}, \frac{h}{k}\right) + A_2^3 * \varepsilon^{II}\left(\frac{k}{\alpha_1}, \frac{h}{k}\right) + A_3^3\right) \tag{41}$$

Integrals $\int X_i d\hat{x}_i, (i,j=1,2,3)$ in Eqs. (32) and (34) are evaluated as:

$$\begin{aligned}
\int X_i d\hat{x}_i &= \int \hat{x}_i \left(A_1^i * \varepsilon^I\left(\frac{k}{\alpha_1},\frac{h}{k}\right) \right. \\
&\left. + A_2^i * \varepsilon^{II}\left(\frac{k}{\alpha_1},\frac{h}{k}\right) + A_3^i \right) d\hat{x}_i \\
&= \frac{1}{2}\hat{x}_i^2 \left(A_1^i * \varepsilon^I\left(\frac{k}{\alpha_1},\frac{h}{k}\right) + A_2^i * \varepsilon^{II}\left(\frac{k}{\alpha_1},\frac{h}{k}\right) + A_3^i \right) \\
&- \int \frac{\hat{x}_i^2}{2} \frac{\partial\left(A_1^i * \varepsilon^I\left(\frac{k}{\alpha_1},\frac{h}{k}\right) + A_2^i * \varepsilon^{II}\left(\frac{k}{\alpha_1},\frac{h}{k}\right) + A_3^i \right)}{\partial \hat{x}_i} d\hat{x}_i \\
&= \frac{\hat{x}_i^2}{2} \left(A_1^i * \varepsilon^I\left(\frac{k}{\alpha_1},\frac{h}{k}\right) + A_2^i * \varepsilon^{II}\left(\frac{k}{\alpha_1},\frac{h}{k}\right) + A_3^i \right) \\
&- \int \frac{(\alpha_1^2 - l_i^2)}{2} \\
&\times \left(1 - \sum_{j\neq i}\left(\frac{\hat{x}_j^2}{\alpha_1^2 - l_j^2}\right)\right) \\
&\frac{\partial\left(A_1^i * \varepsilon^I\left(\frac{k}{\alpha_1},\frac{h}{k}\right) + A_2^i * \varepsilon^{II}\left(\frac{k}{\alpha_1},\frac{h}{k}\right) + A_3^i \right)}{\partial \alpha_1} \frac{\partial \alpha_1}{\partial \hat{x}_i} d\hat{x}_i
\end{aligned} \tag{42}$$

where $l_1 = 0, l_2 = h$ and $l_3 = k$. After evaluating $\partial\alpha_1/\partial\hat{x}_i$ $\partial\alpha_1/\partial\hat{x}_i$ from Eq. (36), the integrals are restated as

$$\begin{aligned}
\int X_i d\hat{x}_i = &\frac{\hat{x}_i^2}{2}\left\{ A_1^i * \varepsilon^I\left(\frac{k}{\alpha_1},\frac{h}{k}\right) + A_2^i * \varepsilon^{II}\left(\frac{k}{\alpha_1},\frac{h}{k}\right) + A_3^i \right\} \\
&- \sum_{j\neq i}\frac{\hat{x}_j^2}{2}\left\{ B_1^{ij} * \varepsilon^I\left(\frac{k}{\alpha_1},\frac{h}{k}\right) + B_2^{ij} * \varepsilon^{II}\left(\frac{k}{\alpha_1},\frac{h}{k}\right) + B_3^{ij} \right\} \\
&- \frac{1}{2}\left\{ C_1^i * \varepsilon^I\left(\frac{k}{\alpha_1},\frac{h}{k}\right) + C_2^i * \varepsilon^{II}\left(\frac{k}{\alpha_1},\frac{h}{k}\right) + C_3^j \right\}
\end{aligned} \tag{43}$$

The first superscript i in B_k^{ij} corresponds to the respective the Lame functions $s_1(j=1)$, $c_1(j=2)$ and $d_1(j=3)$, while the second superscript correspond to the Cartesian coordinate $\hat{x}_j$. Maxwell stress functions are subsequently derived by substituting Eq. (43) in Eqs. (32) and (34) as

$$\begin{aligned}
\Phi_{ll}^{X_i} = &\sum_{j=1}^{3}\frac{\hat{x}_j^2}{2}\left\{ B_1^{ij} * \varepsilon^I\left(\frac{k}{\alpha_1},\frac{h}{k}\right) + B_2^{ij} * \varepsilon^{II}\left(\frac{k}{\alpha_1},\frac{h}{k}\right) + B_3^{ij} \right\} \\
&- \frac{1}{2}\left\{ C_1^i * \varepsilon^I\left(\frac{k}{\alpha_1},\frac{h}{k}\right) + C_2^i * \varepsilon^{II}\left(\frac{k}{\alpha_1},\frac{h}{k}\right) + C_3^j \right\} \forall l = 1,2,3
\end{aligned} \tag{44}$$

The functional forms of B_k^{ij} and C_k^i are determined from the displacement potentials X_1, X_2 and X_3 using the symbolic manipulator MAPLE [43]. The coefficients corresponding to the standard elliptic integrals (i.e. B_k^{ij} and C_k^i for $k = 1,2$ & $i,j = 1,2,3$) are functions of the dimensions of the ellipsoid $f(h,k)$.

The expressions in Eq. (44) should be effectively represented in the stress functions of the Voronoi cell FEM formulation, with two characteristics, viz. : *(i)* The effect of the leading order term should be pronounced at the interface, i.e. at $\alpha_1 = 1$, and should decay rapidly with increasing distance from the interface, i.e. $\alpha_1 \to \infty$; and (*ii*) The resulting stress field should be invariant with respect to coordinate transformations and be independent of the relative orientation of the principal axes of the ellipsoid with respect to the load directions. To achieve the first condition, the elliptic integrals in equation (44) are expanded in a series in α_1 as:

$$\begin{aligned}
\varepsilon^I\left(\frac{k}{\alpha_1},\frac{h}{k}\right) = &\frac{k}{\alpha_1} + \frac{k^3 - kh^2}{6\alpha_1^3} \\
&+ \left(-\frac{1}{20}k^3h^2 + \frac{3}{40}k^5 - \frac{1}{40}kh^4 \right)\alpha_1^{-5} \\
&+ \left(-\frac{3}{112}k^5h^2 - \frac{1}{112}k^3h^4 + \frac{5}{112}k^7 \right. \\
&\left. - \frac{1}{112}kh^6 \right)\alpha_1^{-7} \\
&+ \left(-\frac{5}{1152}kh^8 - \frac{5}{288}k^7h^2 + \frac{35}{1152}k^9 \right. \\
&\left. - \frac{1}{192}k^5h^4 - \frac{1}{288}k^3h^6 \right)\alpha_1^{-9} + O(\alpha_1^{-11}) \\
\varepsilon^{II}\left(\frac{k}{\alpha_1},\frac{h}{k}\right) = &\frac{k}{\alpha_1} + \frac{kh^2 + k^3}{6\alpha_1^3} \\
&+ \left(\frac{1}{20}k^3h^2 + \frac{3}{40}kh^4 - \frac{3}{40}k^5 \right)\alpha_1^{-5} \\
&+ \left(-\frac{3}{112}k^3h^4 - \frac{3}{112}k^5h^2 + \frac{5}{112}kh^6 \right. \\
&\left. - \frac{5}{112}k^7 \right)\alpha_1^{-7} \\
&+ \left(-\frac{35}{1152}k^9 + \frac{5}{288}k^3h^6 + \frac{35}{1152}kh^8 \right. \\
&\left. + \frac{1}{64}k^5h^4 + \frac{5}{288}k^7h^2 \right)\alpha_1^{-9} + O(\alpha_1^{-11})
\end{aligned} \tag{45}$$

Convergence of the series in Eq. (45) is guaranteed, since $h < k < 1$. The rate of convergence is fairly rapid for ellipsoids with low aspect ratio. For example, if the principal axes ratio is $2 : 1.5 : 1$ ($h = 0.661$ and $k = 0.866$), the series expansion takes the form

$$\begin{aligned}
\varepsilon^I\left(\frac{k}{\alpha_1},\frac{h}{k}\right) = &\frac{0.866000}{\alpha_1} + \frac{0.056283649}{\alpha_1^3} + \frac{0.022033934}{\alpha_1^5} \\
&+ \frac{0.0104981217}{\alpha_1^7} + \frac{0.00554282513}{\alpha_1^9} + O\left(\frac{1}{\alpha_1^{11}}\right) \\
\varepsilon^{II}\left(\frac{k}{\alpha_1},\frac{h}{k}\right) = &\frac{0.86600}{\alpha_1} + \frac{0.1602036493}{\alpha_1^3} + \frac{0.05663792256}{\alpha_1^5} \\
&+ \frac{0.02506215896}{\alpha_1^7} + \frac{0.0125602296}{\alpha_1^9} \\
&+ O\left(\frac{1}{\alpha_1^{11}}\right)
\end{aligned}$$

For low aspect ratios, the stress functions in equation (44) can then be expanded in the form $\sum_i(\frac{a_i}{\alpha_1^i})$, where a_i are expansion coefficients. However, for higher aspect ratios, the rate of convergence of ε^{II} is much slower. For example, for the principal axes ratio 9 : 3 : 1 ($h = 0.9439$ and $k = 0.9939$), the series expansion takes the form

$$\varepsilon^I\left(\frac{k}{\alpha_1},\frac{h}{k}\right)=\frac{0.9939315872}{\alpha_1}+\frac{0.0160354296}{\alpha_1^3}+\frac{0.00927200612}{\alpha_1^5}+\frac{0.006386476357}{\alpha_1^7}+\frac{0.00479290549}{\alpha_1^9}+O\left(\frac{1}{\alpha_1^{11}}\right)$$

$$\varepsilon^{II}\left(\frac{k}{\alpha_1},\frac{h}{k}\right)=\frac{0.993931587}{\alpha_1}+\frac{0.31126624}{\alpha_1^3}+\frac{0.175693615}{\alpha_1^5}+\frac{0.11821546}{\alpha_1^7}+\frac{0.08672541547}{\alpha_1^9}+O\left(\frac{1}{\alpha_1^{11}}\right)$$

Comparison of the coefficients of α^{-9} in expressions of ε^{II} for high and low aspect ratios confirm this observation.

To enhance the convergence rate with increasing aspect ratio ellipsoids i.e. for $k \to 1, (0 < h/k < 1)$, the following two limiting functions are added to the series of reciprocal basis functions in α_1 in Eq. (45).

$$limit_{\frac{h}{k}\to 1}\varepsilon^{II}\left(\frac{k}{\alpha_1},\frac{h}{k}\right)=\tanh^{-1}\left(\frac{k}{\alpha_1}\right) \text{ and}$$
$$limit_{\frac{h}{k}\to 0}\varepsilon^{II}\left(\frac{k}{\alpha_1},\frac{h}{k}\right)=\sin^{-1}\left(\frac{k}{\alpha_1}\right) \quad (46)$$

The corresponding linear combination of the two elliptic integrals is

$$A_1*\varepsilon^I\left(\frac{k}{\alpha_1},\frac{h}{k}\right)+A_2*\varepsilon^{II}\left(\frac{k}{\alpha_1},\frac{h}{k}\right)\approx\sum_{i=1}^{n}\frac{a_i}{\alpha_1^i}+b_1\tanh^{-1}\left(\frac{k}{\alpha_1}\right)+b_2\sin^{-1}\left(\frac{k}{\alpha_1}\right) \quad (47)$$

The coefficients B_3^{ij} in Eq. (44) can similarly be represented as a convergent reciprocal series, i.e. $B_3^{ij}=\sum_k\frac{c_k}{\alpha_1^k}$. Again, the rate of convergence of the series is slow for ellipsoids with high aspect ratio, i.e. $(h,k)\to 1$ as $\alpha_1 \to 1$. Consequently, this functional form of B_3^{ij} is retained in the finite element approximation of the stress functions.

The stress functions in Eq. (44) are written in terms of local coordinates $\hat{x}_i, (i = 1,2,3)$ oriented along the ellipsoid principal axes. For representing in terms of global coordinates $x_i, (i = 1,2,3)$, the local coordinates should be transformed to global coordinates according to the relation $(\hat{x}_i = l_i x_1 + m_i x_2 + n_i x_3)$, where $l_i, m_i, n_i, (i = 1,2,3)$ are the direction cosines of the principal axes. Consequently, each of the polynomial terms in the stress function containing $\hat{x}_i^2$ should be replaced by terms containing global coordinates as $x_1^p x_2^q x_3^r$ where the exponents p, q, r are integers satisfying $p + q + r = 2$. Equation (44) can be rewritten for ellipsoids of any orientation as:

$$\Phi_{ll}^{X_i}=\sum_{j=1}^{3}\sum_{\forall p+q+r=2}(c_{pqr}x_1^p x_2^q x_3^r)\times\frac{(B_1^{ij}*\varepsilon^I\left(\frac{k}{\alpha_1},\frac{h}{k}\right)+B_2^{ij}*\varepsilon^{II}\left(\frac{k}{\alpha_1},\frac{h}{k}\right)+B_3^{ij})}{2}-\frac{(C_1^{i}*\varepsilon^I\left(\frac{k}{\alpha_1},\frac{h}{k}\right)+C_2^{i}*\varepsilon^{II}\left(\frac{k}{\alpha_1},\frac{h}{k}\right)+C_3^{j})}{2}\forall l=1,2,3 \quad (48)$$

For incorporation in the finite element formulation, these stress functions are approximated by using series expansion of the elliptic integrals in Eq. (48) as:

$$\Phi_{ll}^{X_i}\approx\sum_{i=1}^{n}\sum_{\forall p+q+r=0}^{2}\frac{\beta_{pqri}x_1^p x_2^q x_3^r}{\alpha_1^i}+\sum_{\forall p+q+r=0}^{2}x_1^p x_2^q x_3^r\beta_{pqr}^1\tanh^{-1}\left(\frac{k}{\alpha_1}\right)+\sum_{\forall p+q+r=0}^{2}x_1^p x_2^q x_3^r\beta_{pqr}^1\sin^{-1}\left(\frac{k}{\alpha_1}\right)+\sum_{\forall p+q+r=0}^{2}x_1^p x_2^q x_3^r\sum_{ij}\beta_{pqr}^{ij}B_3^{ij} \quad (49)$$

The effect of adding the reciprocal functions to the stress functions on the solution convergence is demonstrated in table 2 of section 5.3.

3.1.3
Boundary displacement assumptions

The faces of each 3D Voronoi cell element are generated to be planar polygons. Each face is further dissected into triangular subdomains with a node at the centroid, as shown in Fig. (4)a. The number of triangles is equal to the number of edges on each face. This facilitates interpolation of element boundary displacements. Similarly, the matrix-inclusion ellipsoidal interface is divided into 6 or 24 surface quadrilateral elements. Compatible displacement fields satisfying inter-element continuity on the element boundary $\partial\Omega_e^E$ and inter-phase continuity on the matrix-inclusion interface $\partial\Omega_e^I$ are generated by interpolation of nodal displacements, [18,19] as:

$$\mathbf{u}_e^E = [\mathbf{L}^E]\{\mathbf{q}_e^E\} \text{ on } \partial\Omega_e^E \text{ and } \mathbf{u}_e^I = [\mathbf{L}^I]\{\mathbf{q}_e^I\} \text{ on } \partial\Omega_e^I \quad (50)$$

where $\mathbf{q}_e^E$ and $\mathbf{q}_e^I$ are generalized displacement vectors at the nodes of the element boundary and interface respectively. This is discussed further in section 2.

3.2
Weak form resulting from element assumptions

Substituting Eq. (24) and (50) in the energy functional (17) and setting the first variations with respect to the stress parameters $\{\boldsymbol{\beta}_e^M\}$ and $\{\boldsymbol{\beta}_e^I\}$ respectively to zero, yields the weak forms of the kinematic relations (19),

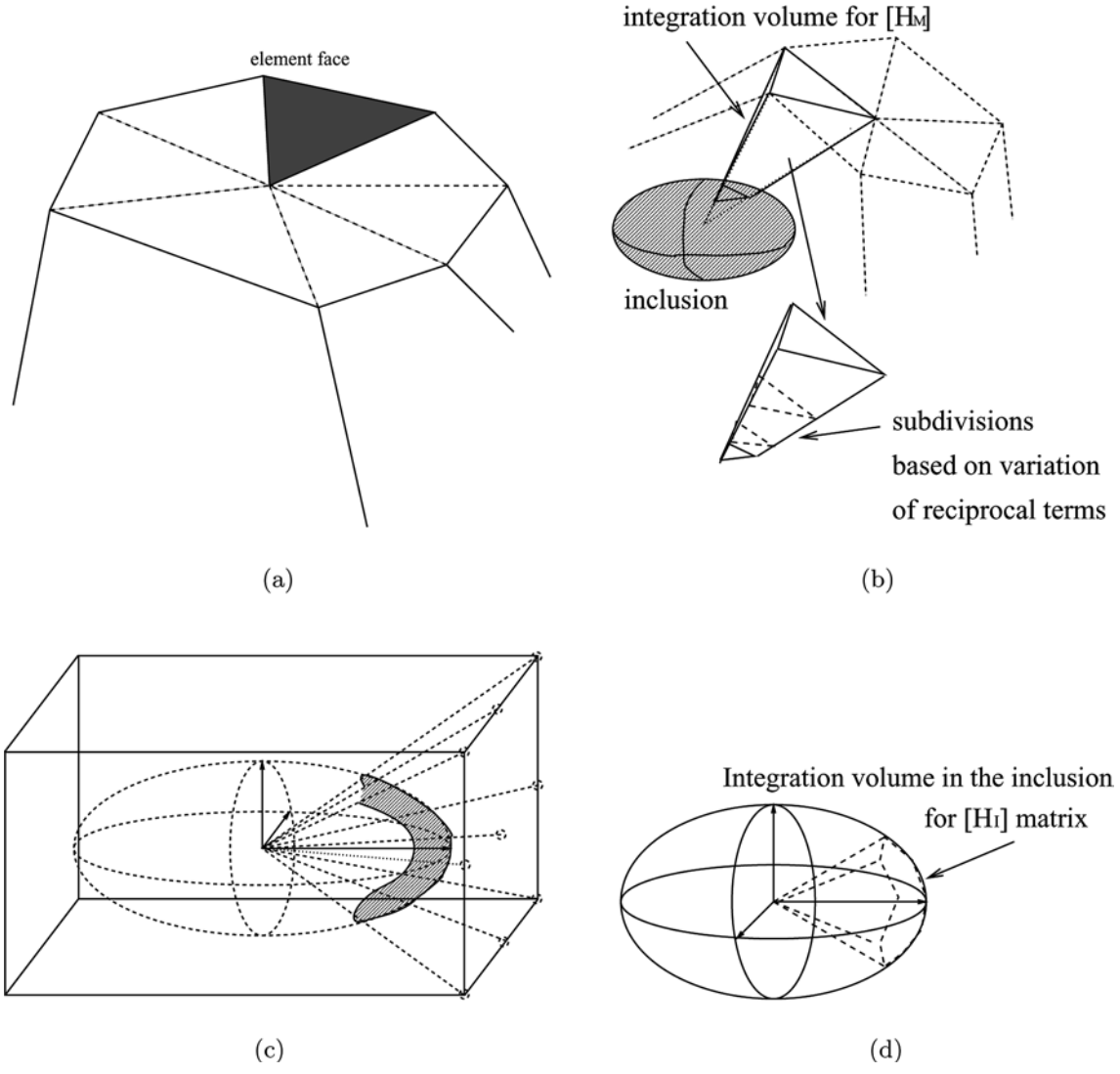

Fig. 4. Element and inclusion surface patches and integration volume: (a) element face patch; (b) integration volume for matrix domain; (c) inclusion surface patch; (d) integration volume for inclusion

$$\int_{\Omega_e^M}[\mathbf{P}^M]^T[\mathbf{S}^\mathbf{M}][\mathbf{P}^M]d\Omega\{\beta_e^M\}=\int_{\partial\Omega_e^E}[\mathbf{P}^M]^T[\mathbf{n}^E][\mathbf{L}^E]d\Omega\{\mathbf{q}_e^E\}-\int_{\partial\Omega_e^I}[\mathbf{P}^M]^T[\mathbf{n}^I][\mathbf{L}^I]d\Omega\{\mathbf{q}_e^I\}\quad(a)$$

$$\int_{\Omega_e^I}[\mathbf{P}^I]^T[\mathbf{S}^\mathbf{I}][\mathbf{P}^I]d\Omega\{\beta_e^I\}=\int_{\partial\Omega_e^I}[\mathbf{P}^I]^T[\mathbf{n}^I][\mathbf{L}^I]d\Omega\{\mathbf{q}_e^I\}\quad(b)\tag{51}$$

where $[\mathbf{n}^E]$ and $[\mathbf{n}^I]$ are the matrices containing components of the unit normals to the element boundary and interface. The kinematic Eq. (51) can be expressed as the matrix equations

$$\begin{bmatrix}\mathbf{H}_M & \mathbf{0}\\ \mathbf{0} & \mathbf{H}_I\end{bmatrix}\begin{Bmatrix}\boldsymbol{\beta}_e^M\\ \boldsymbol{\beta}_e^I\end{Bmatrix}=\begin{bmatrix}\mathbf{G}_E & -\mathbf{G}_{MI}\\ \mathbf{0} & \mathbf{G}_{II}\end{bmatrix}\begin{Bmatrix}\mathbf{q}_e^E\\ \mathbf{q}_e^I\end{Bmatrix}\forall e=1\cdots N\tag{52}$$

Subsequently, setting the first variation of the total energy functional Π with respect to $\{\mathbf{q}_e^E\}$ and $\{\mathbf{q}_e^I\}$ to zero, results in the weak form of the traction reciprocity conditions.

$$\sum_{e=1}^{N}\begin{bmatrix}\int_{\partial\Omega_e^E}[\mathbf{L}^E]^T[\mathbf{n}^E]^T[\mathbf{P}^M]d\Omega & \mathbf{0}\\ -\int_{\partial\Omega_e^I}[\mathbf{L}^I]^T[\mathbf{n}^I]^T[\mathbf{P}^M]d\Omega & \int_{\partial\Omega_e^I}[\mathbf{L}^I]^T[\mathbf{n}^I]^T[\mathbf{P}^I]d\Omega\end{bmatrix}\times\begin{Bmatrix}\boldsymbol{\beta}_e^M\\ \boldsymbol{\beta}_e^I\end{Bmatrix}=\sum_{e=1}^{N}\begin{Bmatrix}\int_{\Gamma_{te}}[\mathbf{L}^E]^T\{\bar{\mathbf{t}}\}d\Omega\\ \{\mathbf{0}\}\end{Bmatrix}\tag{53}$$

Substituting Eq. (52) in the global traction reciprocity Eq. (53), yields the matrix equation:

$$\sum_{e=1}^{N}\begin{bmatrix}\mathbf{G}_E & -\mathbf{G}_{MI}\\ \mathbf{0} & \mathbf{G}_{II}\end{bmatrix}^T\begin{bmatrix}\mathbf{H}_M & \mathbf{0}\\ \mathbf{0} & \mathbf{H}_I\end{bmatrix}\times\begin{bmatrix}\mathbf{G}_E & -\mathbf{G}_{MI}\\ \mathbf{0} & \mathbf{G}_{II}\end{bmatrix}\begin{Bmatrix}\mathbf{q}_e^E\\ \mathbf{q}_e^I\end{Bmatrix}=\sum_{e=1}^{N}\begin{Bmatrix}\int_{\Gamma_{te}}[\mathbf{L}^M]^T\{\bar{\mathbf{t}}\}d\Omega\\ \mathbf{0}\end{Bmatrix}\tag{54}$$

With known tractions and displacements on Γ_{te} and Γ_{ue} respectively, the global traction reciprocity condition (54) is solved for the generalized displacements.

3.3
Stability and convergence

Stability and convergence conditions for displacement-based and stress-based finite element approximations have been developed extensively in [44,45]. Stability conditions of the independent stress-displacement field variational problem in VCFEM, may be assumed to depend on the condition that energy functionals ${}_e a^{M/I}(\boldsymbol{\sigma}_e^{M/I}, \boldsymbol{\sigma}_e^{M/I})$ and ${}_e b_{E/I}^{M/I}(\mathbf{u}_e^{E/I}, \boldsymbol{\sigma}_e^{M/I})$ in equation (18) are positive for all nontrivial stresses and non-rigid body displacements. The bilinear form ${}_e a^{M/I}$ represents the element complimentary energy and may be represented in terms of the stress coefficients from equations (52) and (20) as

$$ {}_e a^{M/I}(\boldsymbol{\sigma}_e^{M/I}, \boldsymbol{\sigma}_e^{M/I}) = < \boldsymbol{\beta}_e^{M/I}, \mathbf{H}_{M/I} \boldsymbol{\beta}_e^{M/I} > \forall \boldsymbol{\sigma}_e^{M/I} \in \mathcal{T}_e^{M/I} \quad (55) $$

where $< . >$ represents the L_2 vector inner product. Consequently, ${}_e a^{M/I}$ is positive for all $\boldsymbol{\sigma} \neq 0$, provided the matrix $[\mathbf{H}]$ is positive definite. From the definition of $[\mathbf{H}]$ in Eqs. (51) and(52), the necessary condition for it to be positive definite is that the compliance tensor $[\mathbf{S}]$ be positive definite, which is true for elastic problems. A second condition is that the finite-dimensional subspaces $\mathcal{T}_e^{M/I}$ be spanned uniquely by the basis functions $[\mathbf{P}^M(x,y,z)]$ and $[\mathbf{P}^I(x,y,z)]$. This is satisfied by assuring linear independence of the columns of basis functions $[\mathbf{P}^M(x,y,z)]$ and $[\mathbf{P}^I(x,y,z)]$, which also guarantees the invertibility of $[\mathbf{H}]$. Furthermore, additional stability conditions should be satisfied to guarantee non-zero stress parameters $\boldsymbol{\beta}_e^{M/I}$ in ${}_e a^{M/I}$ for all non-rigid body boundary displacement fields $\mathbf{u}_e^{E/I}$. This is accomplished by careful choice of the dimensions of the stress and displacement subspaces. From Eqs. (18) and (20), the bilinear forms of the energy functional ${}_e b_{E/I}^{M/I}$ may be represented in terms of the stress and displacement parameters as

$$ \begin{aligned} {}_e b_E^M(\boldsymbol{\sigma}_e^M, \mathbf{u}_e^E) &= < \mathbf{G}_E \mathbf{q}_e^E, \boldsymbol{\beta}_e^M >, \\ {}_e b_I^M(\boldsymbol{\sigma}_e^I, \mathbf{u}_e^I) &= < \mathbf{G}_{MI} \mathbf{q}_e^I, \boldsymbol{\beta}_e^M >, \text{ and} \\ {}_e b_I^I(\boldsymbol{\sigma}_e^I, \mathbf{u}_e^I) &= < \mathbf{G}_{II} \mathbf{q}_e^I, \boldsymbol{\beta}_e^I > \forall \boldsymbol{\sigma}_e^{M/I} \in \mathcal{T}_e^{M/I} \text{ and} \\ & \quad \forall \mathbf{u}^{E/I} e \in \mathcal{V}_e^{E/I} \end{aligned} \quad (56) $$

It is necessary that all these functionals ${}_e b_{E/I}^{M/I} = 0$ for rigid body displacement modes $\mathbf{u}^{E/I}$ on the element boundary and interface. Thus, displacement fields in ${}^{\perp}\mathcal{V}_e^{E/I}$ that are orthogonal to the subspace of rigid body modes, should strictly produce positive strain energies. This discrete L-B-B condition [45,46], ensures stability of multi-field variational problems such as in VCFEM.

3.3.1
Voronoi cell elements with voids

The strain energy for a Voronoi cell element with a void is expressed from Eqs. (20), (56) and (52) as

$$ \begin{aligned} (SE)_e^M &= {}_e\, \mathrm{a}_e^M(\boldsymbol{\sigma}_e^M, \boldsymbol{\sigma}_e^M) = {}_e\, b_E^M(\boldsymbol{\sigma}_e^M, \mathbf{u}_e^E) - {}_e\, b_I^M(\boldsymbol{\sigma}_e^M, \mathbf{u}_e^I) \\ &= < \mathbf{G}_E \mathbf{q}_e^E, \boldsymbol{\beta}_e^M > - < \mathbf{G}_{MI} \mathbf{q}_e^I, \boldsymbol{\beta}_e^M > \\ &= < (\mathbf{G}_E \mathbf{q}_e^E - \mathbf{G}_{MI} \mathbf{q}_e^I), \boldsymbol{\beta}_e^M > \\ &= < [\mathbf{G}_E \quad -\mathbf{G}_{MI}] \begin{Bmatrix} \mathbf{q}_e^E \\ \mathbf{q}_e^I \end{Bmatrix}, \\ & \quad [\mathbf{H}_M]^{-1} [\mathbf{G}_E \quad -\mathbf{G}_{MI}] \begin{Bmatrix} \mathbf{q}_e^E \\ \mathbf{q}_e^I \end{Bmatrix} \\ &= < \left[\mathbf{G}^{void}\right]\{\mathbf{Q}\}, [\mathbf{H}_M]^{-1} \left[\mathbf{G}^{void}\right]\{\mathbf{Q}\} > \end{aligned} \quad (57) $$

For the porous element, $[\mathbf{G}^{void}]$ is a $n_\beta^M \times (n_q^E + n_q^I)$ rectangular matrix, where $n_\beta^M = dim(\mathcal{T}_e^M)$, $n_q^E = dim(\mathcal{V}_e^E)$ and $n_q^I = dim(\mathcal{V}_e^I)$. Since $[\mathbf{H}_M]$ is positive definite, the strain energy in the Voronoi cell element vanishes for zero stress fields in the matrix, and consequently in Eq. (57)

$$ (SE)_e^M = 0 \Leftrightarrow \left[\mathbf{G}^{void}\right]\{\mathbf{Q}\} = 0 \quad (58) $$

The necessary condition of stability is written from Eq. (58) as

$$ [\mathbf{G}^{void}]\{\mathbf{Q}\} = [\mathbf{U}][\boldsymbol{\lambda}][\mathbf{V}]\{\mathbf{Q}\} \neq 0, \forall \mathbf{Q} \bigcap \mathbf{Q}^{rb} = \emptyset \quad (59) $$

where $\mathbf{Q}^{rb}$ correspond to the six rigid body modes of displacement. The matrices $[\mathbf{U}]$ and $[\mathbf{V}]$, whose columns are the eigenvectors of $[\mathbf{G}^{void}][\mathbf{G}^{void}]^T$ and $[\mathbf{G}^{void}]^T[\mathbf{G}^{void}]$ respectively, are orthonormal matrices obtained by singular value decomposition of $[\mathbf{G}^{void}]$. $[\lambda]$ is a rectangular matrix with positive entries on the diagonal corresponding to the square roots of the non-zero eigenvalues of both $[\mathbf{G}^{void}][\mathbf{G}^{void}]^T$ and $[\mathbf{G}^{void}]^T[\mathbf{G}^{void}]$. Premultiplying both sides of Eq. (59) by $[\mathbf{U}]^{-1}$ yields

$$ [\boldsymbol{\lambda}][\mathbf{V}]\{\mathbf{Q}\} = [\boldsymbol{\lambda}]\{\mathbf{Q}^*\} = 0 \quad (60) $$

Since the columns of $[\mathbf{V}]$ are linearly independent, the above equation can only be satisfied for either trivial or rigid body solutions of the boundary displacement. Equation (58) also leads to the L-B-B condition for rank sufficiency of a Voronoi cell element with a void. Positive singular values of $[\boldsymbol{\lambda}]$ imply that the strain energy associated with the stress field solution $\boldsymbol{\sigma}_e^M(\mathbf{u}_e^E, \mathbf{u}_e^I)$ associated with non-rigid body displacement fields $\mathbf{u}_e^{E/I} \in^{\perp} \mathcal{V}_e^{E/I} \forall^{\perp} \mathcal{V}_e^{E/I} \bigcap^{rb} \mathcal{V}_e^{E/I} = \emptyset$ is strictly non-zero. From Eqs. (20) and (58), the L-B-B condition may be stated as:

$$ \begin{aligned} & \exists \gamma > 0 \text{ such that } \sup_{\forall \mathbf{u}_e^{E/I} \in^{\perp} \mathcal{V}_e^{E/I}} \frac{{}_e b_E^M(\boldsymbol{\sigma}_e^M, \mathbf{u}_e^E) - {}_e\, b_I^M(\boldsymbol{\sigma}_e^M, \mathbf{u}_e^I)}{\| \mathbf{u}_e^E \otimes \mathbf{u}_e^I \|} \\ & \quad \geq \gamma \| \boldsymbol{\sigma}_e^M \| \forall \boldsymbol{\sigma}_e^M \in \mathcal{T}_e^M \end{aligned} \quad (61) $$

where $\| \cdot \|$ are metric norms defined in the respective subspaces. The corresponding necessary condition for stability in terms of the matrix dimensions become

$$ n_{\boldsymbol{\beta}}^M > n_q^E + n_q^I - 6 \quad (62) $$

The sufficient condition for stability is established by ensuring that the eigen-values in $[\boldsymbol{\lambda}]$ are positive, which is enforced at the solution stage.

3.3.2
Voronoi cell elements with inclusions

For a composite Voronoi cell element with an embedded inclusion, positiveness of the total strain energy

$(SE)_e = (SE)_e^M + (SE)_e^I$ can be stated in a similar manner as:

$$\exists \gamma > 0 \text{ such that } \sup_{\forall \mathbf{u}_e^E \in^{\perp} \mathcal{V}_e^E} \frac{{}_e b_E^M(\boldsymbol{\sigma}_e^M, \mathbf{u}_e^E)}{\| \mathbf{u}_e^E \|} \geq \gamma \| \boldsymbol{\sigma}_e^M \| \forall \boldsymbol{\sigma}_e^M \in \mathcal{T}_e^M \text{ and}$$

$$\sup_{\forall \mathbf{u}_e^I \in^{\perp} \mathcal{V}_e^I} \frac{{}_e b_I^I(\boldsymbol{\sigma}_e^I, \mathbf{u}_e^I)}{\| \mathbf{u}_e^I \|} \geq \gamma \| \boldsymbol{\sigma}_e^I \| \forall \boldsymbol{\sigma}_e^I \in \mathcal{T}^I \tag{63}$$

The corresponding L-B-B condition or the necessary condition for stability are (see [18,19])

$$n_\beta^M > n_q^E - 6 \text{ and } n_\beta^I > n_q^I - 6 \tag{64}$$

These conditions are sufficient to guarantee the existence of solution and its convergence for multi-field saddle point problem posed by the Voronoi cell FEM with elastic constituents [46].

4 Numerical implementation

4.1 Scaling of the stress function

It is desirable that matrices $[\mathbf{H}_M]$ and $[\mathbf{H}_I]$ have good condition numbers and are invertible. Global cartesian coordinate representation with varying exponents make disparate contributions to these matrices. For example, for $x, y, z >> 1$, different exponents n can make big differences in the matrix components that can lead to bad conditioning with poor invertibility. Scaling of stress functions have been proposed in [18,19] through local element coordinates (ξ, η, ζ). Coordinates (x, y, z) are linearly mapped as

$$\xi = \frac{(x - x_c)}{l}, \eta = \frac{(y - y_c)}{l}, \zeta = \frac{(z - z_c)}{l} \tag{65}$$

where (x_c, y_c, z_c) are the center coordinates of the Voronoi cell element and l is a scaling length determined as:

$$l = \max | \max(x_e - x_c), \max(y_e - y_c), \max(z_e - z_c) | \forall (x_e, y_e, z_e) \in \Omega_e$$

The scaled coordinates are in the range of -1 to 1 for most Voronoi cell elements. The corresponding matrix stress functions in Eq. (49) have the form

$$\Phi_{ij} = \sum_{p+q+r=1}^{m} \xi^p \eta^q \zeta^r \beta_{pqr} + \sum_{p+q+r=1}^{m} \xi^p \eta^q \zeta^r \times \sum_{k=1}^{n} \frac{1}{\alpha_1^{p+q+r+k}} \beta_{pqrk}^m, i = j = 1, 2, 3 \tag{66}$$

4.2 Numerical integration schemes for G and H matrices

4.2.1 Integration of [G] matrices

In Eqs. (52) and (54), the matrices $[\mathbf{G}_{MI}]$ and $[\mathbf{G}_{II}]$ are numerically integrated over the interface and the matrix $[\mathbf{G}_E]$ over the element boundary. All numerical integrations are executed using Gaussian quadrature. VCFEM elements have polygonal boundaries, which are divided into 6 noded quadratic triangular elements as shown in Fig. 4a. For each polygonal face the triangular elements are constructed with one node at the centroid and two others coinciding the vertices of the edges. For the ellipsoidal interface, subdivision to construct 9-noded quadratic elements is done in the following sequence (see Fig. 4c).

1. A bounding box with its edges parallel to the principle axes of the ellipsoids and completely encompassing the ellipsoids is constructed. The ratio of the three edges of the box is the same as the ratio of the three axes of the ellipsoid.
2. 9 nodal points are inscribed on each face of the bounding box. This includes 4 corner nodes, 4 middle nodes and 1 center node.
3. Each of the 9 nodes are joined with the center of the bounding box and the corresponding intercepts with the interface form the quadrilateral surface element. This is repeated for all the 6 faces of the bounding box faces. It provides smaller elements in regions of higher curvature

The $[\mathbf{G}_{II}]$ matrix, requiring integrating over ellipsoidal surface segments of the interface, is sensitive to the surface elements used for the integration. Standard 9 noded-biquadratic elements with isoparametric shape functions can result in significant deviation from the actual surface area especially in regions of high curvature. To overcome this, a parametric equation for the ellipsoid is expressed as

$$x = a \cos\theta \sin\phi, y = b \sin\theta \cos\phi, z = c \cos\phi \tag{67}$$

where a, b, c are the semi-axes and $0 \leq \theta \leq 2\pi$, $-\frac{1}{2}\pi \leq \phi \leq \frac{1}{2}\pi$ correspond to the angular range of the surface. The nodal coordinates are represented as $(\theta_\alpha, \phi_\alpha)$ with $\alpha = 1 \ldots 9$. The Gauss integration points in this mapping are interpolated from the spherical coordinates of the nodes

$$\theta = \sum_{\alpha=1}^{9} N_\alpha \theta_\alpha \phi = \sum_{\alpha=1}^{9} N_\alpha \phi_\alpha$$

where N_α is the interpolation function for a 9 noded biquadratic element. Subsequently, the global Cartesian coordinates of the integration points (x, y, z) are expressed in terms of (θ, ϕ) and the semi-axes a, b, c. In the integration scheme, the integral of a function over a segment on the interface $\left(\int_s f(x, y, z) ds\right)$ is written as $\left(\int_{-1}^{1}\int_{-1}^{1} f\, J_1 J_2 d\xi d\zeta\right)$. J_1 and J_2 are the determinants of the Jacobian operators relating the spherical to cartesian coordinates and natural (master) to spherical coordinates respectively.

$$J_1 = \det \begin{bmatrix} \hat{i} & \hat{j} & \hat{k} \\ \frac{\partial x}{\partial \phi} & \frac{\partial y}{\partial \phi} & \frac{\partial z}{\partial \phi} \\ \frac{\partial x}{\partial \theta} & \frac{\partial y}{\partial \theta} & \frac{\partial z}{\partial \theta} \end{bmatrix} = \sin\phi \cos\theta \sqrt{b^2 c^2 \sin^2\phi + a^2 c^2 \sin^2\phi + a^2 b^2}$$

$$J_2 = \det \begin{bmatrix} \sum_{i=1}^{9} N'_{i_\theta} \theta_i & \sum_{i=1}^{9} N'_{i_\theta} \phi_i \\ \sum_{i=1}^{9} N'_{i_\phi} \theta_i & \sum_{i=1}^{9} N'_{i_\phi} \phi_i \end{bmatrix}$$

This mapping scheme guarantees that all integration points are on the actual surface.

4.2.2
Integration of [H] matrices:

For accurate domain integration of matrices $[\mathbf{H}_M]$ and $[\mathbf{H}_I]$, the matrix and inclusion volumes Ω_e^M and Ω_e^I are subdivided into 3D brick and tetrahedral elements respectively. For the matrix domain Ω_m, the following algorithm is adopted.

- Each face on the element boundary $\partial\Omega_e^E$ is subdivided into triangles by joining the face edges to the center of the element as shown in Fig. 4a. The triangles are represented using 9-noded biquadratic elements with collapsed nodes at the central vertex. • Each node of the above triangular element is projected on the interface $\partial\Omega_e^I$. The projected point is the intersection of the line joining the node with ellipsoid centroid, with the interface. This results in a 9-noded element at the interface as shown in Fig. 4b. • The element-pair at the element face and interface are used to generate 18-noded brick elements for volume integration. It is possible that the projected element on the interface is too large due to the relative positioning of the interface in the Voronoi cell. To correct this problem, each of the triangle pair is subdivided into 3 sub-triangles before generating the brick elements. The subdivision is carried out for the following conditions:

$$\frac{\textit{area of projected triangle}}{\textit{interface area}} > \textit{specified tolerance}$$

$$\textit{or}\ \frac{\textit{area of face triangle}}{\textit{element surface area}} > \textit{specified tolerance}$$

The value of the tolerance is set to 4.5%, which is slightly greater than the area ratio generated by a cubic element with a spherical inclusion at the center. • The 18 noded brick elements are further subdivided to enhance the accuracy of integration of the reciprocal function in $[\mathbf{P}^M]$, particularly near the interface. To accomplish this, the projection line from the face node to the inclusion boundary is subdivided into four segments using the ratio of the in ellipsoidal coordinates: $\alpha_1^1 : \alpha_1^2 : \alpha_1^3 : \alpha_1^4 = 1.1 : 1.2 : 1.3 : 1.4$. The resulting 4 brick elements become progressively larger as they move away from the interface is shown in Fig. 4b. • Gauss quadrature rules are used in each brick element for numerical integration.

For volume integration in the inclusion to evaluate $[\mathbf{H}_I]$, tetrahedral elements are used. As shown in 4d, these elements are constructed by joining interface element nodes with the inclusion centroid.

4.3
Implementation of conditions for stability

Linear independence of the columns of $[\mathbf{P}^M]$ and $[\mathbf{P}^I]$ is natural for pure polynomial expansions. However, when reciprocal functions are used, some of the reciprocal terms may be linearly dependent on the polynomial terms. The rank of matrices like $[\mathbf{P}^M]$ is determined *apriori* from the diagonal matrix resulting from a Cholesky factorization of the square matrix

$$[\mathbf{H}_M^*] = \int_{\Omega_e} [\mathbf{P}^M]^T [\mathbf{P}^M] d\Omega \tag{68}$$

Nearly dependent terms in the columns of $[\mathbf{P}^M]$ will result in very small pivots during the factorization process. Corresponding terms in the stress function are dropped to prevent numerical inaccuracies in the inversion $[\mathbf{H}_M]$.

In VCFEM, the interface nodes are in general, not topologically connected to the element boundary nodes. It is necessary to specify rigid-body modes for the displacement field $\{\mathbf{q}^I\}$ on the interface. A simple procedure, corresponding to the constraining selected displacement modes based on the singular value decomposition of matrix $[\mathbf{G}_\mathbf{I}]$, is performed for Voronoi cell elements with inclusions. Singular value decomposition of the matrix $[\mathbf{G}_E] - [\mathbf{G}_{MI}]$, and matrices $[\mathbf{G}_E]$ and $[\mathbf{G}_{II}]$ are performed for Voronoi cell elements with voids and inclusions respectively to satisfy the discrete L-B-B conditions. The number of degrees of freedom n_β^M and n_β^I in the stress functions Φ^M and Φ^I are chosen to satisfy the Eqs. (62) and (64). Zero singular values in the diagonal of the resulting $[\boldsymbol{\lambda}]$ matrix are removed by enriching the corresponding stress function with polynomial terms. Additionally, extremely small eigen-values in $[\boldsymbol{\lambda}]$ may result in inaccurate displacements. This is averted by constraining selected displacements based on the singular value decomposition of $[\mathbf{G}_{MI}]$ or $[\mathbf{G}_{II}]$. The procedure involves re-writing the matrix multiplication as:

$$[\mathbf{G}]\{\mathbf{q}^I\} = [\mathbf{U}][\boldsymbol{\lambda}][\mathbf{V}]\{\mathbf{q}^I\} = [\mathbf{U}][\boldsymbol{\lambda}]\{\mathbf{q}^I\}_{calt} = [\mathbf{G}]_{alt}\{\mathbf{q}^I\}_{alt} \tag{69}$$

Elements in $\{\mathbf{q}_{\text{alt}}^I\}$ corresponding to small eigen-values in $[\boldsymbol{\lambda}]$ are pre-constrained to zero. The process decreases the dimensions of $\mathcal{V}_{eH}^I$ and results in a loss of accuracy. This procedure constrains rigid-body modes on the inclusion interface and also extremely small eigen-values in $[\boldsymbol{\lambda}]$ which causes inaccurate displacements. The rotated $[\mathbf{G}]_{\text{alt}}$ matrix from singular value decomposition is used in the stiffness matrix calculation and the corresponding displacement vector at the interface is $\{\mathbf{q}_{\text{alt}}^I\}$.

5
Numerical examples

A number of linear elastic boundary value problems are numerically solved by the 3D Voronoi cell finite element model to understand its effectiveness in analyzing heterogeneous microstructures. Heterogeneities in the microstructure are in the form of either voids or inclusions of ellipsoidal shapes. The problems solved are divided into two different categories, namely comparison of microscopic VCFEM solutions with: (i) known analytical solutions for simple unit cells; (ii) results using commercial codes for more complex microstructures.

5.1
Stress distribution around a spherical void

The analytical solution for the three-dimensional stresses around a spherical void in an infinite medium under

uniaxial tension ($\sigma_{zz} = 1$) has been provided in Timoshenko and Goodier [1] (section 137). The stress field from a special stress function is superposed on the solutions of a solid bar in tension for this solution. The special stress field matches the stress field for the solid bar on the surface of the sphere and vanishes to zero at infinity. In the VCFEM analysis, a $L \times L \times L$ domain with a single spherical void of radius $r_d = \frac{L}{5}$ is modeled using a single cubic element. The Possion's ratio of the material is relevant to the solution and is taken to be $v = 0.3$. In the VCFEM implementation, linear displacement fields are assumed on the triangular subdomains on each face, while quadratic triangular elements are used for displacement fields on the void surface. The matrix stress function $\Phi^{M}_{poly})_{ij}$ in equation (25) is taken as a fifth order polynomial stress function $p+q+r = 0 \cdots 5, n_{\beta}^{poly} = 336$. The reciprocal stress functions in Eq. (49) is constructed with $i = 1 \cdots 5$ for $p+q+r = 0 \cdots 2$. The axisymmetric stress function used in [1] can be proved to be equivalent to 3D Maxwell stress functions of the form:

$$\Phi_{11} = \left(\frac{x^2+y^2}{\alpha^5} - 2\frac{z^2}{\alpha^5}\right)c + \left(\frac{(2v-1)(x^2+y^2)}{\alpha^3} + \frac{(2v-2)z^2}{\alpha^3}\right)b + \left(\frac{(2v-1)(x^2+y^2)+(2v-2)z^2+(2v-1)(x^2+z^2)+}{\alpha^3}\right)r_d + \left(\frac{(2v-2)y^2+z^2+y^2}{\alpha^3}\right)r_d + \sigma_0 y^2$$

$$\Phi_{22} = \left(\frac{x^2+y^2}{\alpha^5} - 2\frac{z^2}{\alpha^5}\right)c + \left(\frac{(2v-1)(x^2+y^2)}{\alpha^3} + \frac{(2v-2)z^2}{\alpha^3}\right)b + \left(\frac{(2v-1)(x^2+y^2)+(2v-2)z^2+x^2+z^2}{\alpha^3}\right)r_d + \left(\frac{(2v-1)(z^2+y^2)(2v-2)x^2}{\alpha^3}\right)r_d$$

$$\Phi_{33} = \left(\frac{x^2+y^2}{\alpha^5} - 2\frac{z^2}{\alpha^5}\right)c + \left(\frac{x^2+y^2}{\alpha^3}\right)b + \left(\frac{(2v-1)(x^2+y^2)+(2v-2)x^2+(2v-1)(x^2+z^2)}{\alpha^3}\right)r_d + \left(\frac{(2v-2)y^2+x^2+y^2}{\alpha^3}\right)r_d \quad (70)$$

where $\alpha = \frac{\sqrt{x^2+y^2+z^2}}{r_d}$ corresponds to the ellipsoidal coordinate and a, b, c are material constants that can be expressed as,

$$a = \frac{\sigma_0(1-5v)}{4(7-5v)(1-2v)}, b = \frac{5v}{2(7-5v)}, c = \frac{\sigma_0}{2(7-5v)}$$

For this case, the VCFEM stress interpolation function in Eq. (49) matches the theoretical stress function in Eq. (70) exactly. The solution error can therefore be attributed to the error in displacement interpolations on the void and element boundaries produced by the triangular elements and solution error. Different stress components along a line passing through the center of the sphere are plotted in Fig. 5. The dominant stress along this line, perpendicular to the loading direction, is the normal stress in the loading direction. The VCFEM solutions closely match the stresses in [1].

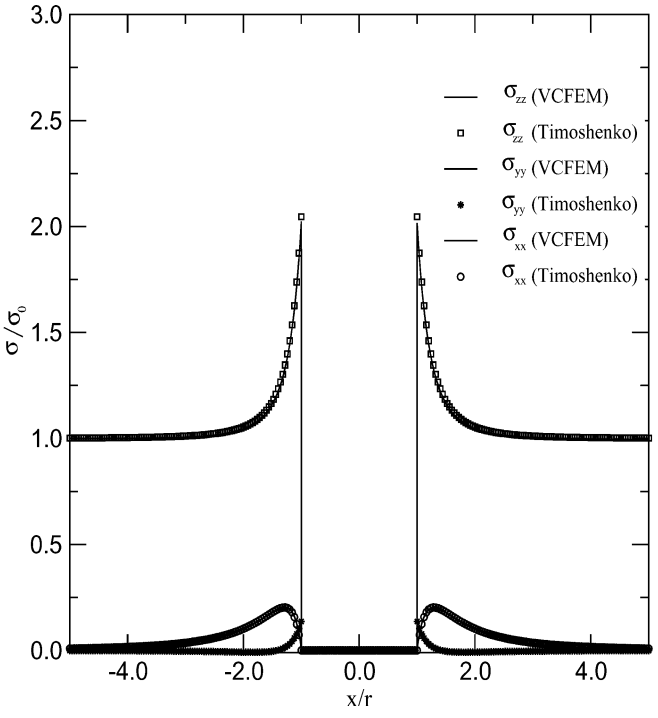

Fig. 5. Comparison of stress distribution along the center line $z = 0$ for the cubical domain with a spherical void

5.2
Stress distribution around an ellipsoidal void

Sadowsky and Sternberg [2] have presented an analytical solution to the problem of stress field around a small ellipsoidal void under uniaxial tension in an infinite medium. The exact solution for stresses is expressed in terms of elliptic functions. In this example, the stress distribution generated by the VCFEM is compared with that in [2]. The ellipsoid has an aspect ratio $a : b : c = 9 : 3 : 1$ in a matrix cube of dimensions $L \times L \times L$, with $L = 5a$. The material properties and the stress and displacement interpolation fields in this problem are same as in the previous example. Stress distributions along the centroidal major axis of the ellipsoid, that is perpendicular to the loading direction are shown in Figs. 6a and b. Concentration of the dominant stress σ_{zz} occurs near the tip of the void on the major axis. The Fig. 6b shows a zoom-in of the stresses near this region. The concentration is very well represented by the VCFEM solution. The slight deviation from the analytical solution, away from the tip, is because of the displacement interpolations on the ellipsoidal surface.

5.3
Effect of interaction of spherical heterogeneities

The interaction between two heterogeneities, which are sources of stress concentration, is of considerable interest to the composites community. Semi-analytical solutions to these problems have been provided in [4] for cavities using bispherical coordinates, and in [5] for rigid inclusions and cavities based on the Boussinesq-

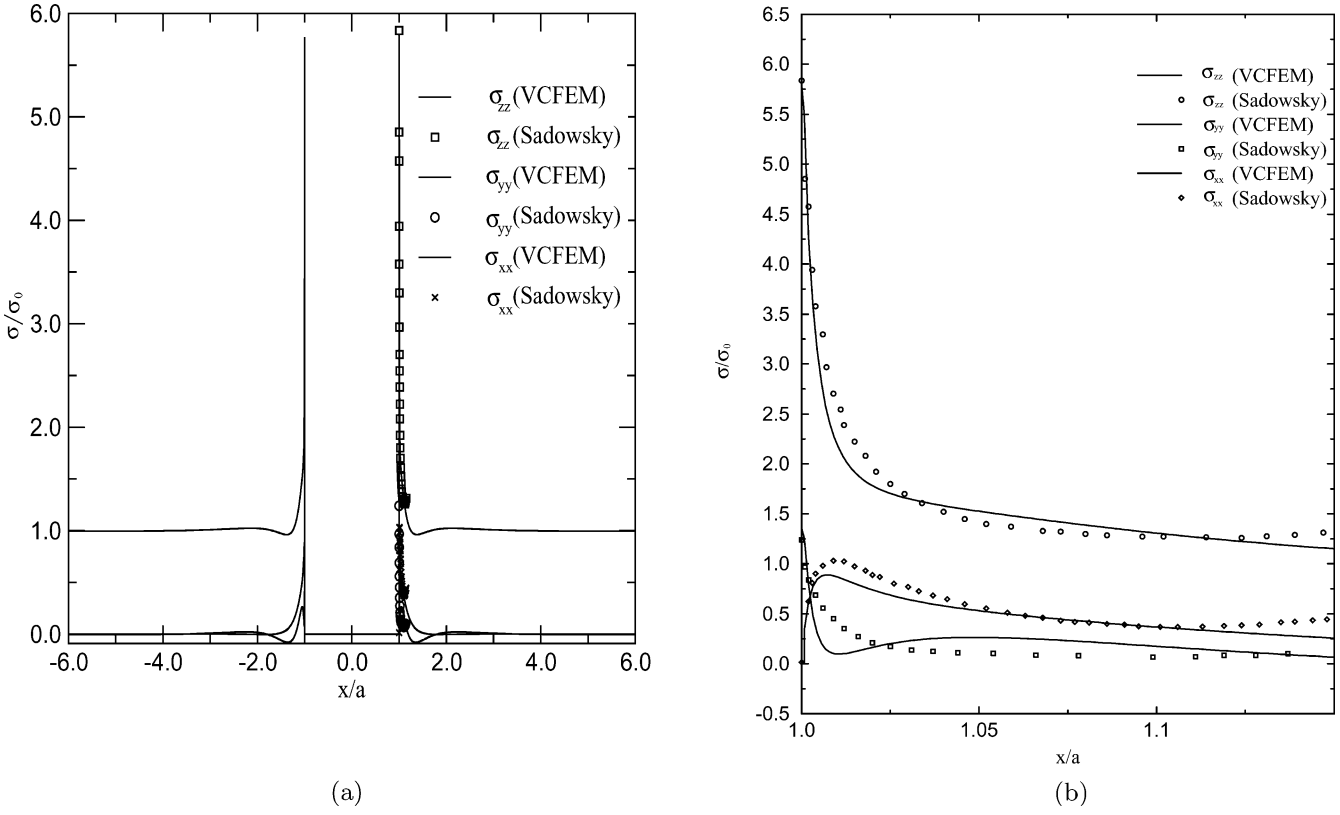

Fig. 6. Comparison of stress distribution along the center line $y = 0, z = 0$ for a cubical matrix with an elliptical void: (a) for different values of x and (b) near the tip of the elliptical void

Papkovich stress functions. The solutions in the latter method are expanded in series of spherical harmonics with respect to the centers of the heterogeneities. The VCFEM implementation involves a mesh of two cubic elements, with each element containing a spherical inclusion or void. The problem is analyzed with the heterogeneities approaching each other and hence the common edge shared by the elements. The stress concentration at the interface increases with decreasing distance. For improved accuracy, the adaptive scheme developed in [19] is implemented to enhance the displacement interpolation using $h-p$ enrichment. The error indicator for adaptation is based on the traction discontinuity along the element boundary and the heterogeneity-matrix interface. Once identified for refinement, the boundaries and interfaces are successively subdivided into smaller triangles till the traction reciprocity error is within acceptable tolerance.

The first problem solved using VCFEM involves two voids of radius r, whose centroids are separated by a distance R. The distance is set to $R = 4r$ in this problem. The boundary condition corresponds to a far field hydrostatic tension of $\sigma^{\infty}_{xx} = \sigma^{\infty}_{yy} = \sigma^{\infty}_{zz} = 1$. Stresses generated by VCFEM at the equators and poles of the spheres are compared with analytical solutions of [4] in table 1. The maximum difference between the two solutions is found to be less than 1% .

In the second problem set considered, the two heterogeneities are assumed to be either voids or rigid inclusions. The rigid material is simulated in VCFEM with a very high modulus, corresponding i.e. $E_{inclusion} = 50E_{matrix}$. Two different applied far field strains are considered for generating the solutions suggested in [5]. They are:

(i) A far field hydrostatic tension, represented by the strain field $\epsilon^{\infty}_{xx} = \epsilon^{\infty}_{yy} = \epsilon^{\infty}_{zz} = 1$.
(ii) A far field in-plane tension and out-of-plane compression, represented by the strain field $\epsilon^{\infty}_{xx} = \epsilon^{\infty}_{yy} = -\epsilon^{\infty}_{zz} = 1$. The R/r ratio is varied from 0 to 3 in this problem. Figures 7 shows the comparison of VCFEM results with those in [5] for the normalized stress field σ_{zz} along a line joining the centers of the spheres for $R/r = 3$. A good agreement of the results is observed with less than 1% .

Table 1. Comparison of VCFEM generated stresses with [?] for two spherical voids in an infinite medium at (a) adjacent pole (b) equator (c) remote pole

Stress	Near Pole		Equator		Remote Pole	
	[4]	VCFEM	[4]	VCFEM	[4]	VCFEM
σ_{xx}	1.570	1.5610	0.000	0.0000	1.510	1.4963
σ_{yy}	1.570	1.5673	1.470	1.4810	1.510	1.4988
σ_{zz}	0.000	0.0000	1.500	1.4922	0.00	0.00

Table 2. Convergence rate of the normalized stress $\frac{\sigma_{zz}-\sigma^{\infty}_{zz}}{\mu_0}$ for purely polynomial (*poly*) vs polynomial+reciprocal (*VC*) stress function at point *A* for 2 spherical inclusions shown in fig(??) with $R/r = 3$ with $\epsilon^{\infty}_{xx} = \epsilon^{\infty}_{yy} = -\epsilon^{\infty}_{zz} = 1$

	$n^{poly}_{\beta} = 336$	$n^{poly}_{\beta} = 468$	$n^{poly}_{\beta} = 620$	$n^{VC}_{\beta} = 574$	[6]
Normalized Stress	−7.567	−7.614	−7.693	−8.343	−8.3588

The convergence rate of the VCFE model using purely polynomial stress functions and the combined polynomial and reciprocal terms are examined for rigid inclusions with $R/r = 3$ in table 2. The rate is very slow with purely polynomial based stress function enrichments. However the addition of the reciprocal terms significantly enhances the convergence rate.

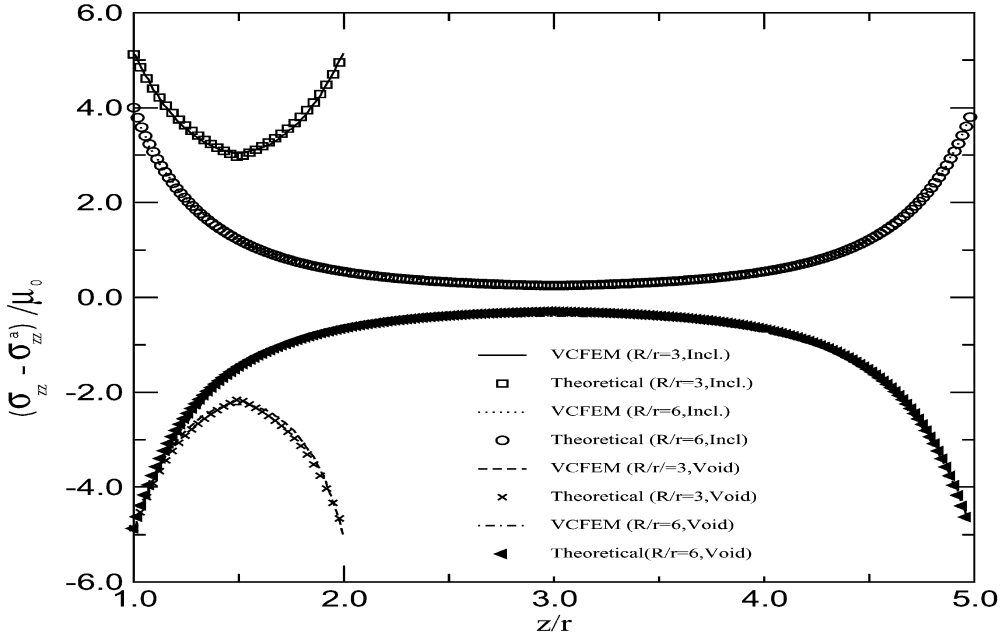

(a)

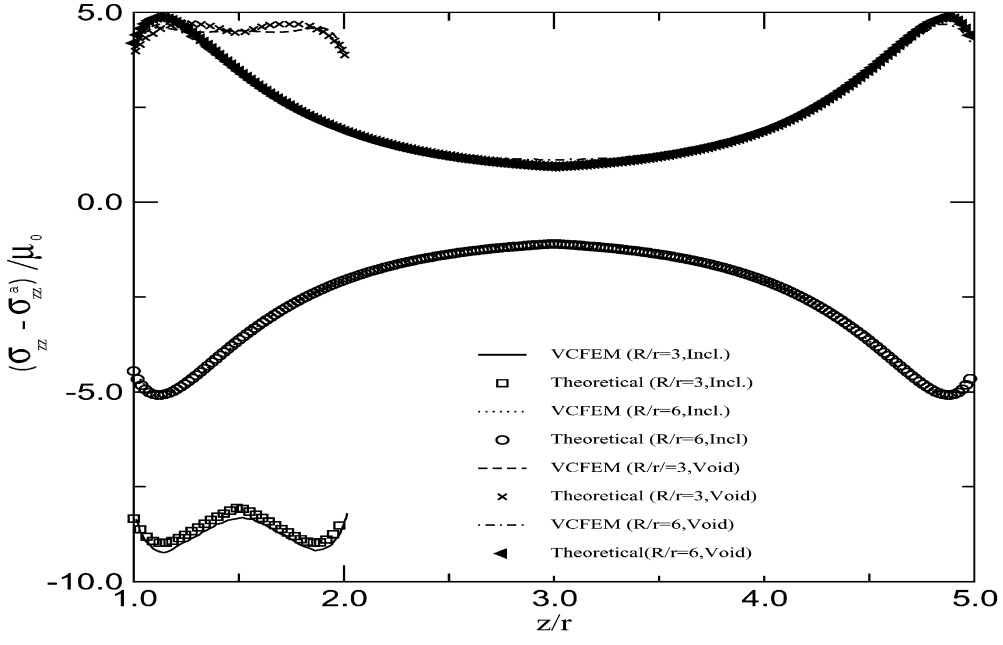

(b)

Fig. 7. Comparison of stress ditribution along the center line bewteen the two spheres, for various values of seperation distance and macroscopic loads with (a) $\epsilon^{\infty}_{ij} = \delta_{ij}$ and (b) $\epsilon^{\infty}_{ij} = \delta_{i1}\delta_{j1} + \delta_{i2}\delta_{j2} - 2\delta_{i3}\delta_{j3}$

5.4
Comparison with ANSYS for random microstructures

A microstructure consisting of randomly dispersed 20 spherical voids in a $10 \times 10 \times 4$ cuboidal matrix ($-5.0 \leq x \leq 5.0; -5.0 \leq y \leq 5.0; 0.0 \leq z \leq 4.0$), is modeled in this example. The microstructure and the Voronoi cell mesh are shown in Fig. 8a, while Fig. 8b shows the mesh with commercial code ANSYS. The VCFEM mesh contains twenty elements corresponding to the number of voids, with a total of 144 nodes on the element boundaries and 1,480 nodes on the matrix-inclusion interfaces. The corresponding converged ANSYS mesh contains 84,123 ten-noded tetrahedron SOLID92 elements and 124,655 nodes. The matrix material has a Young's modulus of $E = 200GPa$ and Poisson's ratio $\nu = 0.3$. The boundary conditions are: (i) Symmetry conditions on faces with $x = -5, y = -5,$ and $z = 0$,; (ii) Displacement $u_z = 4$ on the face $z = 4$, corresponding to an overall strain $\epsilon_{zz} = 1.0$ in the $z-$direction. The other two faces ($x = 5, y = 5$) are traction free. The VCFEM solutions for microstructural stresses are compared to those generated by the highly refined ANSYS model. The tensile stress σ_{zz} along three lines parallel to the coordinate axes x, y, z, and through the origin are plotted in Fig. 9. Stress concentrations of upto 4 are observed along the x and y directions. The VCFEM model is able to capture the important features in the stress distribution with an accurate representation of the peak stresses along the void surface. The bumps and peaks in these plots are due to the unsmoothened representation of matrix stresses resulting in small discontinuities across element boundaries.

5.4.1
Parallel implementation of the VCFEM code

While the 3D VCFEM is accurate for heterogeneous microstructures, it has high requirements of computing time, mainly because of numerical integration using a large number of integration points. A multi-level parallel programming approach is implemented to significantly enhance the computational efficiency of the 3D VCFEM in [47]. The parallelization is conducted for a cluster of symmetric multi-processor (SMP) workstation nodes. MPI is used for data decomposition at a coarse level between the nodes and OpenMP is used for multi-threaded parallelism on each node. The multi-level parallelism combines benefits of improved loop timings and domain decomposition methods to obtain optimized solution times using SMP cluster systems. The code is scalable to any number of multiprocessor nodes such that any number of elements can be solved simultaneously with the only limit being the available hardware resources. The addition of OpenMP directives into the VCFEM model allows for loop level parallelization to occur in an efficient manner. The computations for each element can be performed across multiple processors in a shared memory environment. For the 20-element microstructure, the timings for the multi-level program using different number of nodes of the cluster, with each node running four OpenMP threads, are provided in Fig. 10. Details of the parallelization scheme are provided in [47].

6
Conclusions

A three-dimensional Voronoi cell finite element model (VCFEM) is developed in this paper for analyzing microstructural stresses in elastic domains containing ellipsoidal inclusions or voids. The paper begins with the development of a 3D domain tessellation method for generating the Voronoi cell mesh, in which each Voronoi cell contains one heterogeneity at most. To account for the shapes and sizes of heterogeneities in the domain discretization procedure, a surface-based tessellation algorithm is proposed as a modified form of the point-based tessellation. For planar faces, the surface based tessellation may give rise to

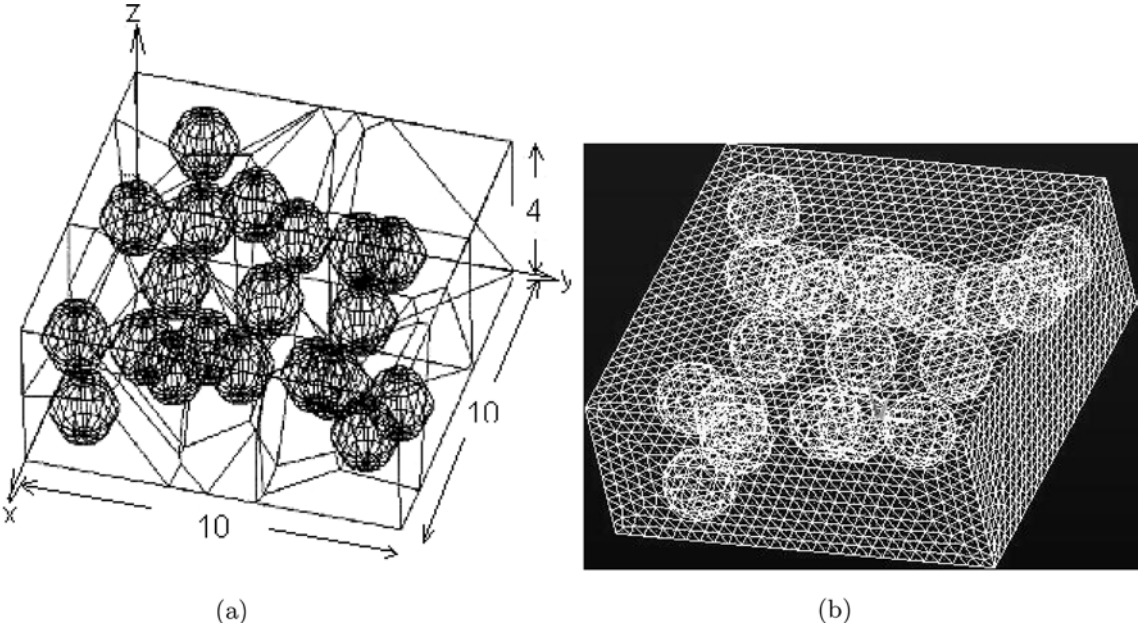

Fig. 8. (a) VCFEM and (b) ANSYS meshes for 20 spherical voids in a cuboidal material domain

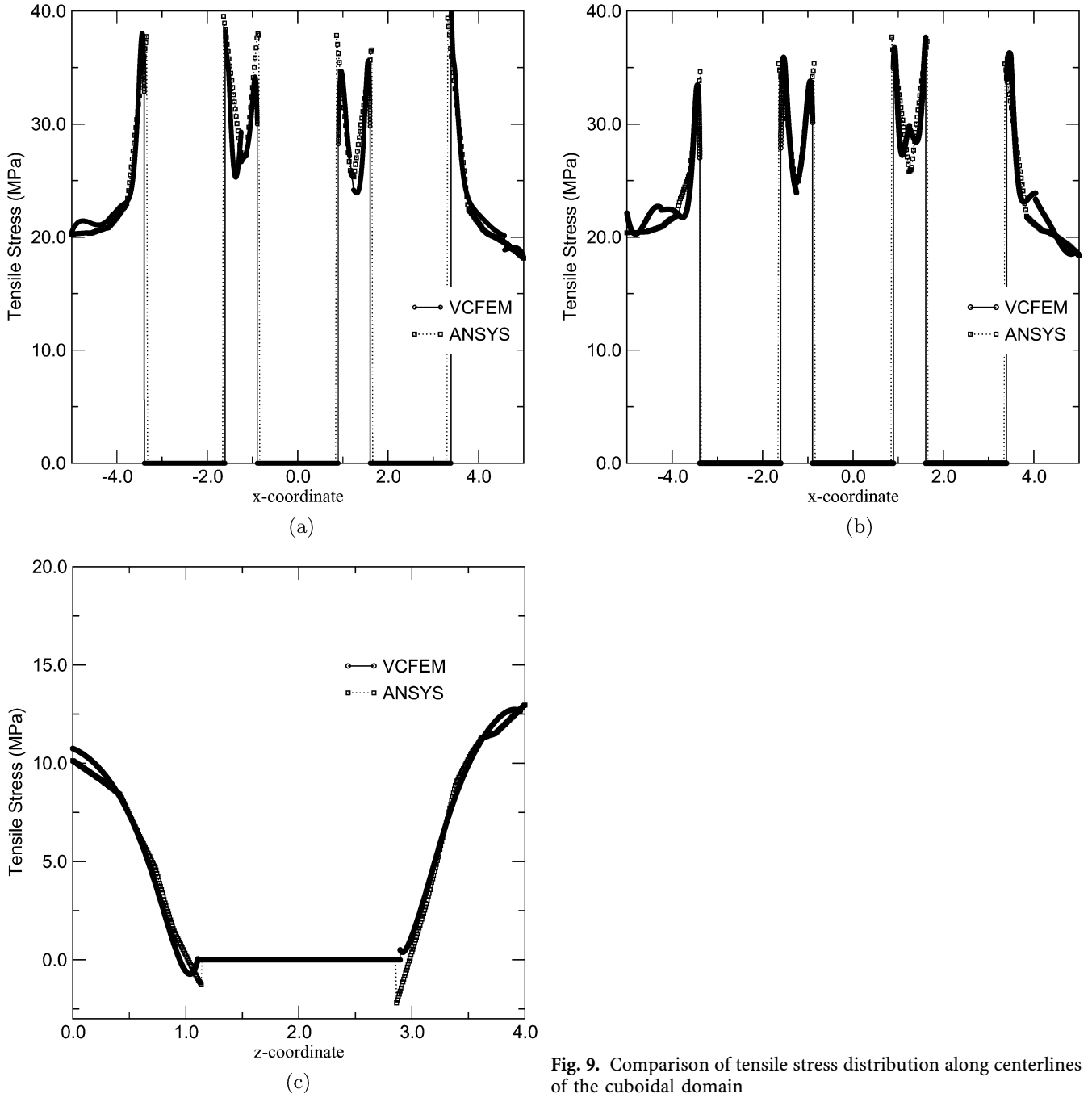

Fig. 9. Comparison of tensile stress distribution along centerlines of the cuboidal domain

non-coinciding triple points. Local adjustments are implemented to avoid such incongruence. The mesh generation algorithm is successfully tested for different microstructures with various shapes, sizes and spatial distribution of heterogeneities.

The Voronoi cell finite element model for small deformation elasticity is subsequently developed using an assumed stress hybrid formulation. In this model, equilibriated stress fields are constructed from symmetric Maxwell or Morera's stress functions. Complete polynomial representation of the stress functions guarantees invariance of stresses with respect to coordinate transformations. A necessary condition for stability is that the columns of the stress interpolation function $[\mathbf{P}(x_1, x_2, x_3)]$. A special procedure of selective elimination of the dependent modes is invoked to restore this condition. Stress functions comprised of pure polynomials yield poor convergence characteristics and consequently special augmentation functions are developed to improve accuracy and efficiency. These functions account for the shape of the interface in its vicinity, but decay with increasing distance from it. Creation of these functions in terms of elliptic integrals and using ellipsoidal harmonics is a major contribution of this paper. The development follows from the derivation of stresses from the general solutions to the Navier's equation. Numerical implementation of the algorithms is presented and especially the methods of filtering out the rigid body modes and enhancing stability

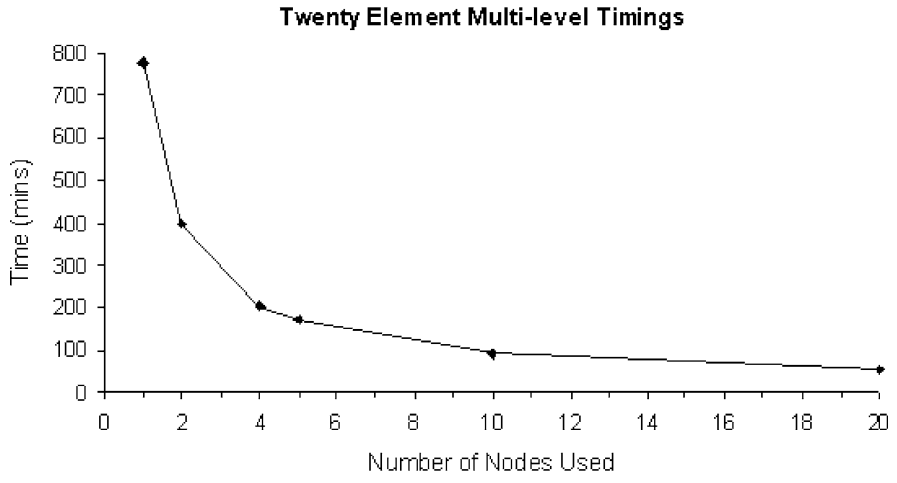

Fig. 10. Speedup with multi-level parallel code with additional computing nodes.

and convergence of the resulting finite element model. Various numerical examples are solved in this paper to validate the model. Comparison of microstructural stress results generated by the 3D VCFEM with analytical solutions in the literature for smaller number of heterogeneities confirm the accuracy of the model. Stress distribution results are also compared with a highly refined FEM model using ANSYS using multiple voids. The accuracy of the VCFEM predictions in these simulations provide adequate validation to the robustness of the formulation. A multi-level code parallelization using Open-MP and MPI adds significant efficiency to the VCFEM simulations.

Three dimensional stress analysis in complex microstructures has currently become a necessity in the design of advanced materials. Despite the disadvantages associated with conventional modeling tools like FEM in efficiently model real microstructures, serious and novel attempts are being made to incorporate three dimensional analyses into practice [8, 9, 10, 13, 14, 15, 16]. The present paper is developed to propose an alternative approach to these developments by way of 3D VCFEM. While this method of modeling with direct interface to the microstructure has considerable promise, a difficulty that is currently faced with, is the large number of integration points needed for the special functions in Gauss quadrature methods. This is a topic of future investigation and reduction.

7 Appendix

7.1 Coefficients for lame and stress functions

The coefficients A_i^j for the lame functions $C_1, S_1 \& D_1$ in equation (40) are given as:

$$A_1^1 = 3h^2, A_2^1 = -3h^2, A_3^1 = 0$$

$$A_1^2 = -\left(1 - \frac{h^2}{k^2}\right)\frac{3hk}{\sqrt{k^2-h^2}}, A_2^2 = \frac{3hk}{\sqrt{k^2-h^2}},$$

$$A_3^2 = -\frac{3h^3}{\sqrt{k^2-h^2}}\frac{\sqrt{\alpha_1^2-k^2}}{\alpha_1\sqrt{\alpha_1^2-h^2}}$$

$$A_1^3 = \frac{3h^2k}{\sqrt{k^2-h^2}}\frac{\sqrt{\alpha_1^2-h^2}}{\alpha_1\sqrt{\alpha_1^2-k^2}},$$

$$A_2^3 = -\frac{3h^2}{\sqrt{k^2-h^2}}, A_3^3 = 0 \tag{71}$$

The coefficients B_k^{ij}, C_k^i for the stress functions in equation (44) are given as

$$B_1^{11} = h, B_1^{12} = -\frac{k^2h}{k^2-h^2}, B_1^{13} = \frac{h^3}{k^2-h^2}$$

$$B_1^{21} = \frac{\sqrt{k^2-h^2}h}{k}, B_1^{22} = -\frac{\sqrt{k^2-h^2}h}{k},$$

$$B_1^{23} = \frac{h^3}{\sqrt{k^2-h^2}k}$$

$$B_1^{31} = \sqrt{k^2-h^2}, B_1^{32} = -\frac{k^2}{\sqrt{k^2-h^2}}, B_1^{33} = 0$$

$$C_1^1 = 0, C_1^2 = 0, C_1^3 = 0$$

$$B_2^{11} = -h, B_2^{12} = h, B_2^{13} = 0$$

$$B_2^{21} = -\frac{\sqrt{k^2-h^2}h}{k}, B_2^{22} = \frac{hk}{\sqrt{k^2-h^2}}, B_2^{23} = 0$$

$$B_2^{31} = -\sqrt{k^2-h^2}, B_2^{32} = \sqrt{k^2-h^2}, B_2^{33} = -\frac{h^2}{\sqrt{k^2-h^2}}$$

$$C_2^1 = h^3, C_2^2 = \frac{\sqrt{k^2-h^2}h^3}{k}, C_2^3 = \sqrt{k^2-h^2}h^2$$

$$B_3^{11} = 0, B_3^{12} = \frac{\sqrt{\alpha_1^2-k^2}h^3k}{\sqrt{\alpha_1^2-h^2}(k^2-h^2)\alpha_1},$$

$$B_3^{13} = -\frac{\sqrt{\alpha_1^2-h^2}h^3k}{\sqrt{\alpha_1^2-k^2}(k^2-h^2)\alpha_1}$$

$$B_3^{21} = 0, B_3^{22} = -\frac{\sqrt{\alpha_1^2-k^2}h^3}{\sqrt{\alpha_1^2-h^2}\sqrt{k^2-h^2}\alpha_1},$$

$$B_3^{23} = -\frac{\sqrt{\alpha_1^2-h^2}h^3}{\sqrt{\alpha_1^2-k^2}\sqrt{k^2-h^2}\alpha_1}$$

$$B_3^{31} = 0, B_3^{32} = \frac{\sqrt{\alpha_1^2-k^2}h^2k}{\sqrt{\alpha_1^2-h^2}\sqrt{k^2-h^2}\alpha_1},$$

$$B_3^{33} = \frac{\sqrt{\alpha_1^2-h^2}h^2k}{\sqrt{\alpha_1^2-k^2}\sqrt{k^2-h^2}\alpha_1}$$

$$C_3^1 = 0, C_3^2 = 0, C_3^3 = 0 \tag{72}$$

References

1. **Timoshenko SP, Goodier JN** (1970) Theory of Elasticity, (McGraw-Hill, U.S.A.)
2. **Sadowsky MA, Sternberg E** (1947) Stress concentration around an ellipsoidal cavity in an infinite body under arbitrary plane stress perpendicular to the axis of revolution of cavity. J. Appl. Mech., Trans. ASME 69:A191–201
3. **Sadowsky MA, Sternberg E** (1949) Stress concentration around a triaxial ellipsoidal cavity. J. Appl. Mech., Trans. ASME A-29:149–157
4. **Sternberg E, Sadowsky MA** (1952) On the axisymmetric problem of the theory of elasticity for an infinite region containing two spherical cavities. J. App. Mech., Trans. ASME A 19:19-27
5. **Chen H-S, Acrivos A** (1978) The solution of the equations of linear elasticity for an infinite region containing two spherical inclusions. Int. J. Solids Struct. 14:331–348
6. **Chen FC, Young K** (1977) Inclusions of arbitrary shape in an elastic medium. J. Math. Phys., 18(7):1412–1416
7. **Agarwal A, Broutman L** (1974) Three dimensional finite element analysis of spherical particle composites. Fib. Sci. Technol. 7:63–77
8. **Banerjee P, Henry D** (1992) Elastic analysis of three–dimensional solids with fiber inclusions, Int. J. Solids Struct. 29:2423–2440
9. **Rodin GJ, Hwang Y** (1989) On the problem of linear elasticity for an infinite region containing a finite number of non-intersecting spherical inhomogeneities. Int. Solids Struct. 27:145–159
10. **Gusev AA** (1997) Representative volume element size for elastic composites: A numerical study. J. Mech. Phys. Solids 45:1449–1459
11. **Zohdi TI** (2001) Computer optimization of vortex manufacturing of advanced materials. Comput. Meth. Appl. Mech. Engng. 190:6231–6256
12. **Michel JC, Moulinec H, Suquet P** (1999) Effective properties of composite materials with periodic microstructure: a computational approach Comput. Meth. Appl. Mech. Engrg. 172:109–143
13. **Böhm HJ, Eckschlager A, Han W, Rammerstorfer FG** (2000) 3D arrangement effects in particle reinforced metal matrix composites. In: A.S. Khan, H. Zhang and Y. Yuan (eds.) Plastic and Viscoplastic Response of Materials and Metal Forming. Neat Press, pp 466–468
14. **Böhm HJ, Eckschlager A, Han W** (1999) Modeling of phase arrangement effects in high speed tool steels. In: F. Jeglitsch, R. Ebner and H. Leitner (eds.) Tool Steels in the Next Century. Montanuniversität Leobe, Leoben Austria, pp 147–156
15. **Segurado J, Llorca J, Gonzalez C**(2002) On the accuracy of mean field approaches to simulate the plastic deformation of composites. Scripta Mater. 46:525–529
16. **Moes N, Cloirec M, Cartraud P, Remacle J-F** (2003) A computational approach to handle complex microstructure geometries. Comput. Meth. Appl. Mech. Engrg. 192:3163–3177
17. **http://www.matsim.ch/PalmyraE.html**
18. **Moorthy S, Ghosh S** (1996) A model for analysis of arbitrary composite and porous microstructures with Voronoi cell finite elements. Int. J. Numer. Meth. Engrg. 39:2363–2398
19. **Moorthy S, Ghosh S** (2000) Adaptivity and convergence in the Voronoi cell finite element model for analyzing heterogeneous materials. Comput. Meth. Appl. Mech. Engrg. 185: 37–74
20. **Ghosh S, Moorthy S** (1998) Particle Cracking Simulation in Non-Uniform Microstructures of Metal-Matrix Composites. Acta Metallurgica et Materillia 46(3):965–982
21. **Moorthy S, Ghosh S** (1998) A Voronoi cell finite element model for particle cracking in composite materials. Comput. Meth. Appl. Mech. Engrg. 151:377–400
22. **Ghosh S, Mukhopadhyay SN** (1991) A two dimensional automatic mesh generator for finite element analysis of random composites. Comput. Struct. 41:245–256
23. **Okabe A, Boots B, Sugihara K** (1992) Spatial tessellations concepts and applications of Voronoi diagrams. John Wiley & Sons ISBN:0 471 93430 5
24. **Kumar S** (1992) Computer Simulation of 3D Material Microstructure and Its Application in the Determination of Mechanical Behavior of Polycrystalline Materials and Engineering Structures. Ph D Dissertation, Penn. State University
25. **Kiang T** (1966) Random fragmentation in two and three dimensions. Z. Astrophys 64:433–439
26. **Andrade PN, Fortes MA** (1988) Distribution of cell volumes in a Voronoi partition. Phil. Mag. B 58:671–674
27. **Mahin KW, Hanson K, Morris JW** (1980) Comparative analysis of the cellular and Johnson-Mehl microstructures through computer simulation. Acta Metall. B 28:443–453
28. **Mackay AL** (1972) Stereological characteristics of atomic arrangements in crystals. J. Microscopy 95(2):217–227
29. **Finney JL** (1979) A procedure for construction of Voronoi polyhedra. J. Comput. Phys. 32:137–143
30. **Tanaka M** (1986) Statistics of Voronoi polyhedra in rapidly quenched monatomic liquids I: Changes during rapid quenching process. J. Phys. Soc. Japan 55:3108–3116
31. **Hinde AL, Miles RE** (1980) Monte-Carlo estimates of the distribution of the random polygons of the Voronoi tessellation with respect to a Poisson process. Stat. Comput. Simul. 10:205–223
32. **Pathak P** (1981) PhD Dissertation, University of Minnesota
33. **Winterfeld PH** (1997) Percolation and Conduction Phenomena in Disordered Composite Media. PhD Dissertation, University of Minnesota
34. **Tuma JJ, Walsh RA**(1997) Engineering Mathematics Handbook. McGraw-Hill, U.S.A ISBN 0 07 065529 4
35. **Dixon LCW, Spedicato E, Szegö GP** (1980) Nonlinear Optimization Theory and Algorithms. Birkhauser ISBN 3 7643 3020 1
36. **Cohen AM, Cutts JF, Fielder R, Jones DE, Ribbans J, Stuart E** (1973) Numerical Analysis. Halsted Press, ISBN 0 470 16423 9
37. **Saada AS** (1993) Elasticity Theory and Applications. 2nd edn. Krieger Publishing Co., Malabar, Florida
38. **Filonenko-Borodich M** (1993) Theory of Elasticity. P. Noordhoff N.V. Scientific Publishers, Groningen, The Netherlands
39. **Spilker RL, Singh SP** (1982) Three-dimensional hybrid-stress isoparametric quadratic displacement elements. Int. J. Numer. Methods Eng. 18:445–465
40. **Muskhelishvili NI** (1965) Some Basic Problems in the Mathematical Theory of Elasticity. P.Nordhoff Ltd., Netherlands
41. **Hobson EW** (1931) The theory of spherical and ellipsoidal harmonics. University Press, Cambridge, England
42. **Abromowitz M, Stegun IA** (1991) Handbook of Mathematical Funtions. Dover Publications, U.S.A.
43. **Kofler M** (1997) Maple Version 5 Release 3: An Introduction and Reference. Addison-Wesley, U.S.A.
44. **Babuska I** (1973) The finite element method with Lagrange multipliers. Numer. Math. 20:179–192
45. **Brezzi F** (1974) On the existence, uniqueness and approximation of saddle-point problems arising from Lagrange Multipliers. R.A.I.R.O 8–R2 pp129–151
46. **Xue W-M, Karlovitz LA, Atluri SN** (1985) On the existence and stability conditions for mixed-hybrid finite element solutions based on Reissner's variational principle. Solids. Struc 21(1):97–116
47. **Eder PE** (2002) High Performance Multi-level parallel Programming for Adaptive Multi-Scale Finite Element Modeling of Composite and Porous Structures. M.S. Thesis, The Ohio State University